



TECHNISCHE
UNIVERSITÄT
WIEN

Vienna University of Technology

Diplomarbeit

Combustion of Hydrocarbon Fuels at Normal and Elevated Pressures

ausgeführt zum Zwecke der Erlangung des akademischen Grades eines
Diplom-Ingenieurs unter der Leitung von

Ao.Univ.Prof. Dipl.-Ing. Dr.techn. Ernst Pucher
E 315 - Institut für Fahrzeugantriebe und Automobiltechnik
Technische Universität Wien

Prof. Dr. Kalyanasundaram Seshadri
Department of Mechanical and Aerospace Engineering
University of California, San Diego, USA

eingereicht an der Technischen Universität Wien
Fakultät für Maschinenwesen und Betriebswissenschaften

von

Mathias Innerkofler
Matrikel Nr.: 1028051
Wachtelweg 17
A-9400 Wolfsberg

Wien, August 2018

Combustion of Hydrocarbon Fuels at Normal and Elevated Pressures

Diploma Thesis

Mathias Innerkofler

Institute of Internal Combustion Engines and Automotive
Engineering

Vienna University of Technology

Advisor:

Ao. Univ-Prof. Dipl.-Ing. Dr.techn. Ernst Pucher
Institute for Powertrains and Automotive Technology
Vienna University of Technology, Austria

Prof. Dr. Kalyanasundaram Seshadri
Department of Mechanical and Aerospace Engineering
University of California, San Diego, USA

San Diego, August 2018

Eidesstattliche Erklärung

Ich erkläre an Eides statt, dass die vorliegende Arbeit nach den anerkannten Grundsätzen für wissenschaftliche Abhandlungen von mir selbstständig erstellt wurde. Alle verwendeten Hilfsmittel, insbesondere die zugrunde gelegte Literatur, sind in dieser Arbeit genannt und aufgelistet. Die aus den Quellen wörtlich entnommenen Stellen, sind als solche kenntlich gemacht.

Das Thema dieser Arbeit wurde von mir bisher weder im In- noch Ausland einer Beurteilerin/einem Beurteiler zur Begutachtung in irgendeiner Form als Prüfungsarbeit vorgelegt.

Wien, August, 2018

Unterschrift

Abstract

An improved understanding of mechanism of autoignition of hydrocarbon fuels and extinction of combustion reactions are of fundamental and practical importance. The practical importance arises from the need to establish limits of operation of energy conversion systems. Autoignition is a key parameter that influences the performance of compression ignition engines. Combustion process in these engines are considered to be nonpremixed because the fuel and air are mixed after they enter the combustion chamber. Numerous studies have addressed autoignition in premixed systems. In comparison there are very few studies of autoignition in nonpremixed systems. For homogeneous premixed systems shock tubes have been used to measure ignition delay times, as a function of temperature and concentration of fuel and oxygen in the reactant mixture. These studies, however, do not address the influences of the flow field. The research described in this thesis is an experimental and computational investigation of the autoignition and extinction of high molecular weight alkanes in laminar, nonpremixed, and nonuniform flows. The experimental part of the work was performed at the University of California at San Diego and the supporting computational work by the CRECK Modelling Group at Politecnico di Milano. The alkanes considered are n-heptane, n-decane, and n-dodecane.

The experimental studies are performed at atmospheric pressure employing the counterflow configuration, because in this configuration the flow field can be accurately characterized. In this configuration two counterflowing streams are directed toward a stagnation plane. One stream, called the fuel-stream, is made up of vaporized fuel mixed with nitrogen and the other stream, called the oxidizer stream, is a mixture of oxygen and nitrogen. The temperature and mass fraction of fuel in the fuel stream are represented by $Y_{F,1}$ and T_1 , respectively, and the temperature and mass fraction of oxygen in the oxidizer stream are represented by $Y_{O_2,2}$ and T_2 , respectively. In the limit of large values of the Reynolds number of the counterflowing streams a thin viscous layer is established in the vicinity of the stagnation plane and chemical reactions are confined to this layer. This viscous layer is bounded by inviscid regions on both sides. The flowfield in the inviscid regions is characterized by the strain rate, a , defined as the gradient of velocity. The strain rate is calculated from injection velocities of the reactant streams using a previously developed asymptotic theory. The

reciprocal of the strain rate is also a measure of the flow time or residence time. The critical conditions of extinction and autoignition depend on $Y_{F,1}$, $Y_{O_2,2}$, T_1 , T_2 and a . A key objective of this work is to elucidate the influence of $Y_{F,1}$, and $Y_{O_2,2}$ on critical conditions of extinction and autoignition. Critical conditions of extinction were measured at fixed values of $Y_{O_2,2} = 0.233$, $T_1 = 533.15 [K]$, $T_2 = 298 [K]$. The strain rate at extinction, a , was measured for various values of $Y_{F,1}$. Critical conditions of autoignition were measured at fixed values of $T_1 = 533.15 [K]$, and $a = 550 [s^{-1}]$. Two sets of experiments were performed; in one set $Y_{O_2,2} = 0.233$ and the temperature of the oxidizer stream T_2 was measured for various values of $Y_{F,1}$ and in the other set of experiments $Y_{F,1} = 0.4$ and the temperature of the oxidizer stream T_2 was measured for various values of $Y_{O_2,2} = 0.233$.

The numerical predictions were carried out using the computer code OpenSMOKE++ that was developed at Politecnico di Milano. The structure of the laminar counterflow flame was described employing one-dimensional conservation equations of mass, momentum and energy, and the balance equation for species mass fractions. The kinetic model was made up of roughly 3000 elementary reactions. Critical conditions of extinction and autoignition were calculated and compared with experimental data. The experimental data and predictions show that the strain rate at extinction increases with increasing values of $Y_{F,1}$. In general, at a given value of $Y_{F,1}$ the predicted value of a is higher than the measurements. The experimental data and predictions show at fixed $Y_{O_2,2}$, the temperature of the oxidizer stream at autoignition decreases with increasing $Y_{F,1}$. In general, at a given value of $Y_{F,1}$, the predicted T_2 is higher than the corresponding measured value. At fixed $Y_{F,1}$, the measurements show that T_2 decreases with increasing $Y_{O_2,2}$, while the calculated value of T_2 is nearly independent of $Y_{O_2,2}$. Further studies are needed to establish the reasons for the differences between predictions and measurements. To elucidate the influence of pressure on critical conditions of autoignition, the temperature of the oxidizer stream was calculated for values of pressure of 1 atm, 5 atm and 10 atm at fixed $a = 550 [s^{-1}]$, $Y_{O_2,2} = 0.233$, and $T_1 = 533.15 [K]$. At a given value of $Y_{F,1}$, the value of T_2 decreases with increasing p .

Kurzfassung

Ein besseres Verständnis des Selbstzündungsmechanismus von Kohlenwasserstoffbrennstoffen und das Auslösen von Verbrennungsreaktionen sind von grundlegender und praktischer Bedeutung. Die praktische Bedeutung ergibt sich aus der Notwendigkeit, die Betriebsgrenzen für Energieumwandlungssysteme festzulegen. Die Selbstzündung eines Gemisches ist ein Schlüsselparаметer in der motorischen Verbrennung, welcher die Leistungsabgabe von Motoren beeinflusst. Der Verbrennungsprozess in diesen Motoren wird als nicht vorgemischte Verbrennung bezeichnet, da der Brennstoff und die Luft erst miteinander vermischt werden, nachdem sie in die Brennkammer injiziert worden sind. In zahlreichen Studien wurde die Selbstentzündung vorgemischter Systeme behandelt. Im Vergleich dazu gibt es nur sehr wenige Studien zur Selbstzündung in nicht vorgemischten Systemen. Für homogene vorgemischte Systeme wurden sogenannte Shock Tubes verwendet, um die Zündverzugszeiten als Funktion der Temperatur und der Konzentration von Kraftstoff und Sauerstoff in der Reaktantenmischung zu messen. Diese Studien befassen sich jedoch nicht mit den Einflüssen des Strömungsfeldes auf die Verbrennungsvorgänge. Die im Rahmen dieser Forschungsarbeit durchgeführten experimentellen und numerischen Untersuchungen beschäftigen sich mit der Selbstzündung und der Auslöschung von Alkanen mit hohem Molekulargewicht in laminaren, nicht vorgemischten Strömungen. Der experimentelle Teil der Arbeit wurde an der University of California San Diego durchgeführt und die unterstützenden Berechnungsergebnisse wurden von der CRECK Modeling Group am Politecnico di Milano bereitgestellt. Die in dieser Arbeit untersuchten Alkane sind n-Heptan, n-Decan und n-Dodecan.

Die experimentellen Untersuchungen werden bei Atmosphärendruck unter Verwendung eines Gegenstrombrenners durchgeführt, da diese Konfiguration eine sehr genaue Charakterisierung des Strömungsfeldes ermöglicht. In diesem Gegenstrombrenner werden zwei Ströme axial symmetrisch ausgerichtet, sodass eine Stagnationsebene zwischen ihnen entsteht. Der Brennstoffstrom besteht aus verdampftem Kraftstoff, der mit Stickstoff gemischt ist und der Oxidationsmittelstrom ist ein Gemisch aus Sauerstoff und Stickstoff. Die Temperatur und der Massenanteil von Kraftstoff im Brennstoffstrom werden durch $Y_{F,1}$ bzw. T_1 dargestellt und die Temperatur und der Massenanteil von Sauerstoff im Oxidationsmittelstrom werden

durch $Y_{O_2,2}$ bzw. T_2 dargestellt. Auf Grund der sehr großen Reynoldszahlen beider Ströme, kommt es in der Nähe der Stagnationsebene zur Bildung einer dünnen viskosen Grenzschicht, auf welcher alle chemischen Reaktionen beschränkt sind. Diese viskose Schicht wird von nichtviskosen Bereichen auf beiden Seiten begrenzt. Das Strömungsfeld in den nichtviskosen Bereichen ist durch die Strain Rate a , die als Geschwindigkeitsgradient definiert ist, gekennzeichnet. Die Strain Rate wird aus den Injektionsgeschwindigkeiten der Reaktandenströme, sowie unter der Verwendung einer zuvor entwickelten asymptotischen Theorie berechnet. Der Kehrwert der Strain Rate ist auch ein Maß für die Fließzeit, oder Verweilzeit der Reaktanten in der Reaktionszone. Die kritischen Auslöschungs- und Selbstzündungsbedingungen hängen von $Y_{F,1}$, T_1 , $Y_{O_2,2}$, T_2 und a ab. Das Hauptziel dieser Forschungsarbeit ist es, den Einfluss von $Y_{F,1}$ und $Y_{O_2,2}$ auf kritische Auslöschungs- und Selbstzündungsbedingungen zu untersuchen und zu analysieren. Die kritischen Bedingungen der Erlöschung der Flamme werden bei Umgebungsdruck, konstantem Sauerstoffanteil $Y_{O_2,2}$ und bei unterschiedlichen Kraftstoffanteilen $Y_{F,1}$ eruiert. Die Temperaturen des Oxidationsmittelstromes bei Selbstzündung werden sowohl bei konstant gehaltenem Kraftstoffmassenanteil $Y_{F,1}$, konstanter Strainrate a_2 und variierendem Sauerstoffanteil $Y_{O_2,2}$, als auch bei konstantem Sauerstoffanteil $Y_{O_2,2}$, konstanter Strainrate a_2 und variierendem Kraftstoffmassenanteil $Y_{F,1}$ aufgezeichnet und ausgewertet.

Die numerischen Berechnungen wurden mit einem am Politecnico di Milano entwickelten Computercode OpenSMOKE ++ durchgeführt. Die Struktur der laminaren Gegenstromflamme wurde unter Verwendung eindimensionaler Erhaltungsgleichungen von Masse, Impuls und Energie und der Ausgleichsgleichung für Massenanteile von Spezies beschrieben. Die kritischen Auslöschungs- und Selbstzündungsbedingungen wurden berechnet und mit den experimentellen Daten verglichen. Die experimentellen Daten und Vorhersagen zeigen, dass die Strain Rate bei einer Auslöschung der Flamme mit steigenden Werten von $Y_{F,1}$ zunimmt. Im Allgemeinen ist bei einem gegebenen Wert von $Y_{F,1}$ der berechnete Wert der Strain Rate höher als die Messungen. Die experimentellen Daten und Vorhersagen zeigen, dass bei festem $Y_{O_2,2}$ die Temperatur des Oxidationsmittelstroms bei Selbstzündung mit zunehmendem $Y_{F,1}$ abnimmt und bei einem gegebenen Wert von $Y_{F,1}$ das

vorhergesagte T_2 höher als der entsprechende gemessene Wert ist. Bei festem $Y_{F,1}$ zeigen die Messungen, dass T_2 mit zunehmendem $Y_{O_2,2}$ abnimmt, während der berechnete Wert von T_2 nahezu unabhängig von $Y_{O_2,2}$ ist. Weitere Studien sind notwendig, um die Gründe für die Unterschiede zwischen den numerischen Berechnungen und Messungen zu ermitteln. Um den Einfluss des Drucks kritischer Bedingungen der Selbstentzündung zu untersuchen, wurde die Temperatur des Oxidationsmittelstroms für Druckwerte von 1 atm, 5 atm und 10 atm bei festem $a = 550 \text{ s}^{-1}$, $Y_{O_2,2} = 0.233$ und $T_1 = 533.15 \text{ [K]}$. Bei einem gegebenen Wert von $Y_{F,1}$ nimmt der Wert von T_2 mit zunehmendem p ab.

Acknowledgements

I welcome this opportunity to express my sincere gratitude to my advisors who offered me to conduct and write my master thesis at the University of California in San Diego.

I would first like to thank Professor Ernst Pucher from the Institute for Powertrains and Automotive Technology of the Technical University of Vienna, for his patient support, encouragement and advice throughout my time as his student. Furthermore, I want to thank Professor Kalyanasundaram Seshadri from the Institute of Mechanical and Aerospace Engineering of the University of California in San Diego for his patience, motivation, and immense knowledge. His guidance helped me in all the time of research and writing of this thesis.

My special words of thanks should also go to my research co-worker Martin Hunyadi-Gall and to the CRECK Modeling Group of Politecnico di Milano for their support, guidance, cooperation and encouragement.

I also want to thank the Austrian Marshall Plan Foundation for their generosity in funding the Austrian Marshall Plan Foundation Scholarship. I am very honored to be one of the recipients of this award. The research at UCSD was supported by the U. S. Army Research Office, Grant # W911NF-16-1-0054 (Program Manager Dr. Ralph A. Anthenien Jr), and the U. S. National Science Foundation Grant # CBET-1404026.

Finally, I must express my very profound gratitude to my family especially my parents, my sister and to my girlfriend Sabrina for providing me with unfailing support and continuous encouragement throughout my years of study and through the process of researching and writing this thesis abroad.

Table of Contents

List of Symbols	VIII
Subscripts	X
Nomenclature	XI
1. Introduction.....	1
2. Fundamentals in Combustion Physics and Chemical Kinetics.....	2
2.1. Combustion of Hydrocarbons	2
2.2. Speed of a Chemical Reaction.....	3
2.3. H ₂ -O ₂ -System	4
2.4. Limit Phenomena of Hydrocarbon Diffusion Flames	6
2.4.1. Principle of the Atmospheric Pressure Counterflow Burner.....	6
2.4.2. Strain Rate.....	8
2.4.3. The S-Curve Concept.....	11
2.4.4. Critical States of Ignition and Extinction	13
2.4.5. Momentum Balance	13
3. Apparatus and Procedure	14
3.1. Tested Fuels	15
3.2. Lower Part of the Burner	16
3.3. Upper Part of the Burner	17
3.4. Vaporizer	19
3.5. LabView Controlling Software	20
3.6. Gas Flow Control and Calibration	22
3.7. Temperature Measurement and Control	23
3.7.1. Temperature Correction	24
3.8. Experimental Procedure.....	26
4. Experimental- and Numerical Results at Atmospheric Pressure	29
4.1. Results of the Autoignition Experiments	29
4.2. Results of the Extinction Experiments.....	37
5. Autoignition of Hydrocarbon Fuels at Elevated Pressures.....	39
5.1. Numerical Results of the Autoignition Event at Elevated Pressures	40
6. Concluding Remarks	41
References.....	i
Figures	iii
APPENDIX.....	vi

List of Symbols

A	Pre-exponential factor or interaction parameter [-]
a	Strain rate [1/s]
b	Temperature exponent [-]
cp	Heat capacity [kJ/kgK]
d	Thermocouple diameter [mm]
Da	Damköhler number [-]
E	Activation Energy [J/mol]
f	Ratio of nondimensional axial velocity to nondimensional temperature
h	Heat transfer rate coefficient [-]
K	Constant
k	Rate constant [-]
k	Thermal conductivity [W/mK]
l	Length [mm]
L	Separation distance [mm]
Nu	Nusselt number [-]
Pr	Prandtl number [-]
p	Pressure [Pa]
\dot{Q}	Heat flow [J/mol]
r	Nondimensional radial coordinate
R	Gas constant [J/molK]
Re	Reynolds number [-]
T	Temperature [K]
U	Function related to radial component of velocity ($=rU$)
u	Velocity [m/s]
u	nondimensional function related to radial component of velocity
v	nondimensional axial component of velocity
V	Axial component of velocity
z	Nondimensional axial coordinate
ϑ	Nondimensional temperature
ν	Stoichiometric coefficients [-]
ε	Emissivity [-]

ρ	Density [kg/m ³]
σ	Stefan -Boltzmann constant [W/m ² K ⁴]
ν	Kinematic viscosity [m ² /s]
μ	Dynamic viscosity [kg/ms]

Subscripts

1	Fuel side
2	Oxidizer side
<i>a, b</i>	Products
<i>c, d</i>	Educts
<i>cat</i>	surface-induced catalytic reactions
<i>cond</i>	Conduction
<i>conv</i>	Convection
<i>rad</i>	Radiation
<i>f</i>	Indices forward reaction
<i>i, j</i>	Species or indices
<i>r</i>	Indices reverse reaction
<i>surr</i>	Surroundings
<i>tc</i>	Thermocouple

Nomenclature

CO	Carbon monoxide
CO_2	Carbon dioxide
H_2O	Water
H_2	Hydrogen
H', HO_2	Radicals
HC	Unburned hydrocarbons
NO	Nitrogen monoxides
N_2	Nitrogen
NO_x	Nitrogen oxides
O_2	Oxygen
O', OH	Radicals

1. Introduction

Modern society is closely linked to the automobile. The need for the automobile is also reflected in the 600 million cars which are on the road worldwide. The majority of these cars are powered by conventional internal combustion engines, which are reciprocating piston engines. These internal combustion engines represent one of the most efficient heat engines on the market. Internal combustion engines are not only used in commercial vehicles, but also in shipping and as generators in power engineering, where depending on the drive concept efficiencies of over 50 percent can be achieved. Latest forecasts show that the number of vehicles will almost double by the middle of the century, from 600 million to about 1.1 billion vehicles. However, this will also result in a steadily growing social and political pressure on the automotive industry in terms of pollutant emissions, recyclability and fuel consumption of newly developed vehicles. The main focus will be on reducing pollutant emissions and CO_2 emissions. The CO_2 emissions released by the combustion of fossil fuels are greenhouse gases and thus jointly responsible for global warming. Road traffic also contributes to global warming and pollution, even though to a limited extent. Combustion of a modern gasoline engine with a 3-way catalytic converter produces about 72.5% N_2 , 13.5% CO_2 , 12.5% H_2O and 0.8% O_2 and other inert gases. Less than 1% of the exhaust gases are considered harmful and are legally limited. Nevertheless, the majority of the population is concerned about the environmental impact of the automobile, as well as its resources and energy consumption.

Conventional combustion engines will continue to dominate as a drive concept in vehicles over the next few decades due to their flexibility, compactness and efficiency. The European Commission has predicted that by 2030, up to 40 percent of all kilometers traveled will be in metropolitan areas. For this purpose, it is necessary to understand the fundamental processes occurring during combustion and to further reduce the resulting pollutants in order to both allow the cleanest possible road traffic, and to continue to ensure an urban habitat in metropolitan areas. The research described here is concerned with fundamental mechanisms of autoignition and extinction studied by employing a counter flow configuration. The thesis involves a theoretical part on combustion physics and chemical kinetics as well as an experimental section on structures of hydrocarbon diffusion flames of vaporized

n-heptane, n-decane and n-dodecane, including experimental measurements and numerical computations with full chemical-kinetic mechanisms.

2. Fundamentals in Combustion Physics and Chemical Kinetics

2.1. Combustion of Hydrocarbons

The exact knowledge of hydrocarbon oxidation kinetics is very important due to the fact that this process is involved in many technological processes. In internal combustion engines, the chemically bond energy is used by the combustion of fuel and oxygen. The combustion of hydrocarbons takes place in chain reactions, which take place in several successive reactions as shown in Figure 1.

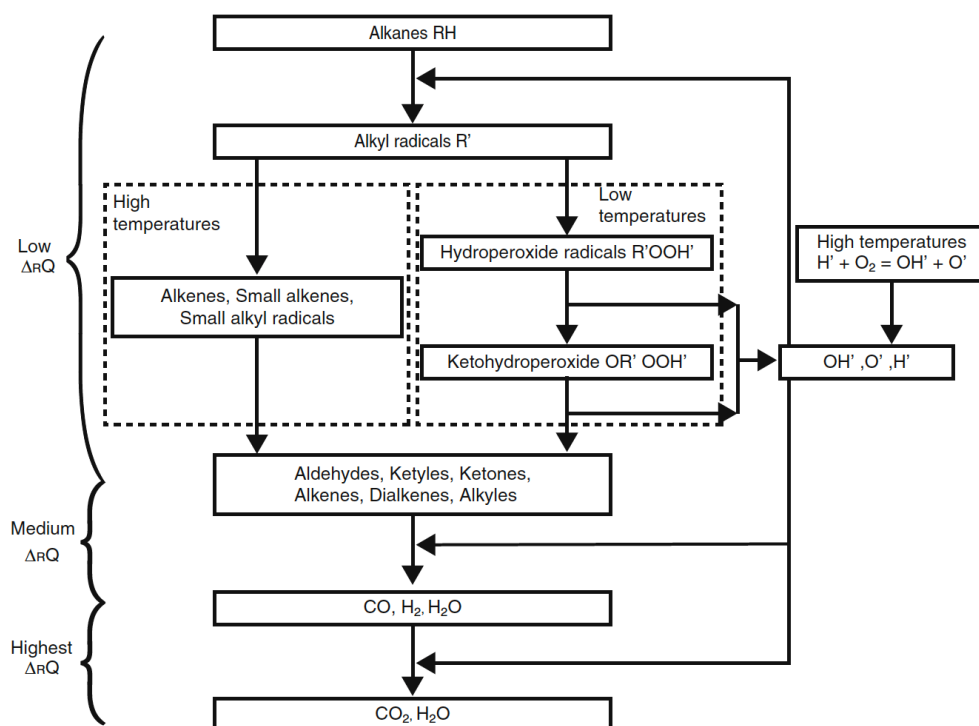


Figure 1: Diagram of the hydrocarbon oxidation process [1]

At both low and high temperatures, a hydrogen atom is separated from the hydrocarbon molecule. At low temperatures so-called hydrocarbon peroxides are formed. These hydrocarbon peroxides break down to smaller hydrocarbons due to oxidation and dehydration [1]. At very high temperatures, the formation of hydrogen peroxides is prevented. This leads to the formation of one alkene and a small alkyl

radical. Subsequent reactions with the radicals H' , O' and OH' form light alkenes and alkadienes and finally aldehydes, such as formaldehyde CH_2O and acetaldehyde CH_3CHO . The formation of aldehydes, which produces only about 10% of the total heat release, is accompanied by the appearance of a cold flame. In the subsequent blue flame CO , H_2 and H_2O and in the final stage of the hot flame CO_2 and H_2O are formed. When the hydrocarbons are oxidized to CO , about another 30% and upon the oxidation of CO to CO_2 , the remaining 60% of the thermal energy which is stored in the fuel is finally released. The essential heat release takes place only at the end of the reaction scheme during the oxidation of CO to CO_2 . [2] [1]

2.2. Speed of a Chemical Reaction

By the following equation, the chemical reaction of reactants (A_a, A_b) into products (A_c, A_d) is described,



The coefficients v_i represent the stoichiometric coefficients of the reaction, respectively. In principle, any chemical reaction can run both forwards as well as backwards, which leads to the following simplified equation,

$$\sum_i v_i A_i = 0. \quad (2.3)$$

The reaction rate describes the speed at which reactants are converted into products. Chemical reactions vary greatly in the speed at which they occur. In general, reaction rates depend on the concentrations of the reacting substances. This phenomenon can be explained by the collision theory for reaction rates. At very high concentrations, there are also numerous molecules in the volume, which leads to frequent collisions. Hence, the reacting molecules transform into the reaction products and the reaction proceeds rapidly. The concentrations of the reactants can be related to the reaction rate by using the so-called rate law. The constant of proportionality k is called the rate constant or the velocity coefficient [3]. For the chemical reaction, which is given in equation 2.2, the change of a species concentration, e.g. A_c , can be given by the following formulation

$$\frac{d[A_c]}{dt} = v_c (k_f [A_a]^{v_a} [A_b]^{v_b} - k_r [A_c]^{v_c} [A_d]^{v_d}) . \quad (2.4)$$

The first term on the right side describes the reaction rate of the forward reaction and the second term the rate of the reverse reaction. The velocity coefficients of the

forward and reverse reactions are indicated by k_f and k_r and they are given by an Arrhenius formulation

$$k = AT^b \exp\left(-\frac{E_A}{RT}\right). \quad (2.5)$$

Where k is the reaction rate constant, A is the pre-exponential factor [$1/K^b s$], b is the temperature exponent $[-]$, T is the absolute temperature $[K]$, R is the gas constant $[J/molK]$ and E_A is the activation energy $[J/mol]$. The formulation shows the dependency of the speed coefficients on the temperature. The activation energy is the minimum amount of energy which must be available to a chemical system with potential reactants to result in a chemical reaction. In Figure 2 the chemical bond energy over the reaction coordinate for the reaction $A + B \rightleftharpoons C + D$ is shown.

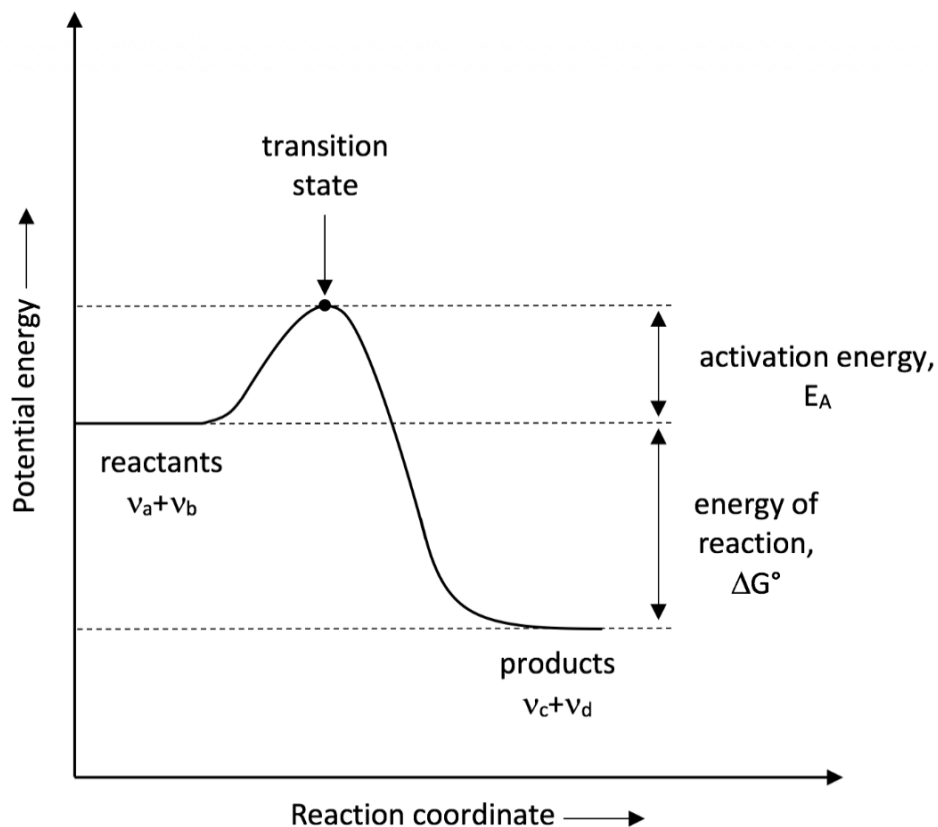


Figure 2: Schematic figure of the chemical bond energy as a function of the reaction coordinate

2.3. H_2 - O_2 -System

The $H_2 - O_2$ system has a simple ignition mechanism and is important for hydrogen combustion studies and also as a subset of the reaction mechanisms of more complex

fuels. The following equations represent the main reactions connected to the ignition event [1],



The radicals $H\dot{O}_2$, OH and H contained in the reaction equations are responsible for driving the reactions. The reaction which is represented by equation 2.8 is a wall termination [1]. Depending on the state variables, pressure and temperature, different chemical reactions take place for a mixture within the ignition limits. These reactions can cause auto-ignition or no ignition. The effect of the different reactions on ignition can be explained by means of an explosion diagram, as it is shown in Figure 3. The $H_2 - O_2$ diagram shows that in the range of very low pressures and constant temperatures no reactions take place, since the radicals formed quickly diffuse to the combustion chamber walls and recombine in a reaction. Increasing the pressure slows down diffusion and causing the chain branches to predominate and the first explosive limit to be reached. Here, a spontaneous ignition of the mixture takes place because the production of radicals exceeds the conversion of these to stable molecules. The equation 2.11 becomes more important and the mixture becomes stable again [1]. A further increase in pressure results in the 2nd explosion limit being reached and the area in which it can be ignited ends. For pressure values in the range between the 2nd and 3rd explosive limit, a preponderance of chain termination reactions, compared to chain branching reactions, prevents a self-ignition of the mixture. At very high-pressure values above the 3rd explosion limit (thermal ignition limit), the mixture ignites again. [2]

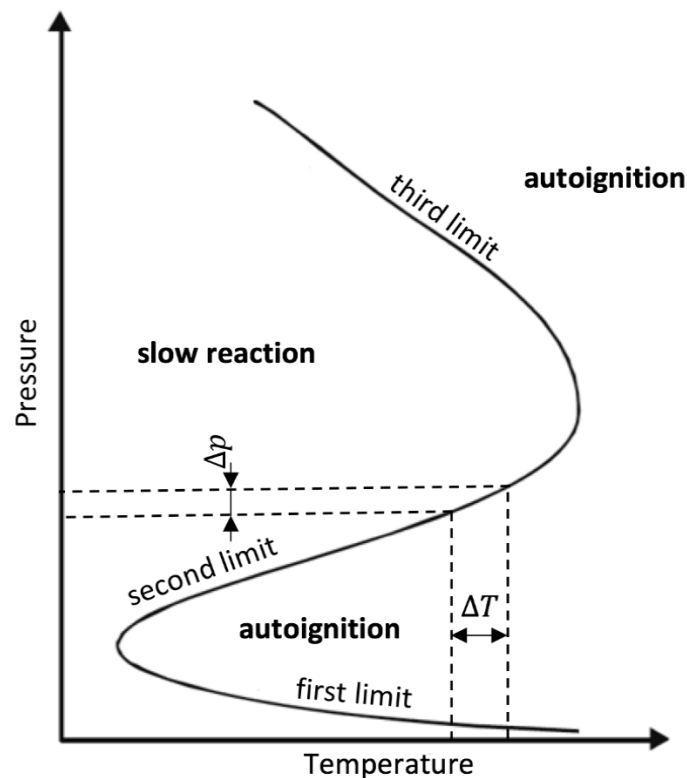


Figure 3: H₂-O₂ explosion diagram

2.4. Limit Phenomena of Hydrocarbon Diffusion Flames

2.4.1. Principle of the Atmospheric Pressure Counterflow Burner

The two basic categories of flame propagation are the premixed and non-premixed propagation. In premixed flames the fuel and the oxidizer are mixed prior the reaction zone. The stoichiometry of the mixture can be controlled by changing the fuel to oxidized ratio, and an inert gas such as nitrogen is used to dilute the reactants and vary the flame temperature. An example where a premixed flame propagation takes place is the combustion chamber of common used gasoline engines. In gasoline engines, the fuel and oxidizer are mixed before they are injected into the cylinder. Diffusion flames or also called non-premixed flames occur when the fuel and oxidizer are not mixed prior to reacting. The oxidizer is supplied from the ambient air and the mixing and combustion reactions take place together [1]. Counterflow diffusion flames in general are very often used experimentally because they are better controllable and stable, and they also represent a one-dimension diffusion flame structure. In Diesel engines for example, the fuel is injected into the cylinder near the top dead center. During the so-called ignition delay time, the fuel atomizes into droplets, vaporizes and

the mixing with air occurs simultaneously until the temperature in the cylinder reaches the fuel ignition temperature [1] [2].

In the present thesis, all experiments are carried out with a non-premixed laminar counterflow setup. The critical conditions of autoignition and extinction are measured employing an atmospheric pressure counterflow burner. This counterflow burner consists of two axisymmetric ducts opposing each other. The lower duct is called the fuel duct, as a mixture of vaporized fuel and nitrogen enters the reaction zone. The upper duct is called the oxidizer duct and guides the oxidizer, which consists of a mixture of pure nitrogen and oxygen, into the reaction zone. Both streams are assumed to be steady, laminar and axisymmetric. A stagnation plane is generated by impinging the uniform oxidizer stream against the uniform fuel stream. In the near of the stagnation plane a thin viscous boundary layer establishes. Due to manually ignition or an autoignition event a flame occurs and stabilizes in the thin viscous layer in the vicinity of this surface if the local mixture fraction gradient is sufficiently high [4]. The combustion in a counter flow burner is mainly dependent on the chemical reaction time, and the flow velocities of the fuel and the oxidizer.

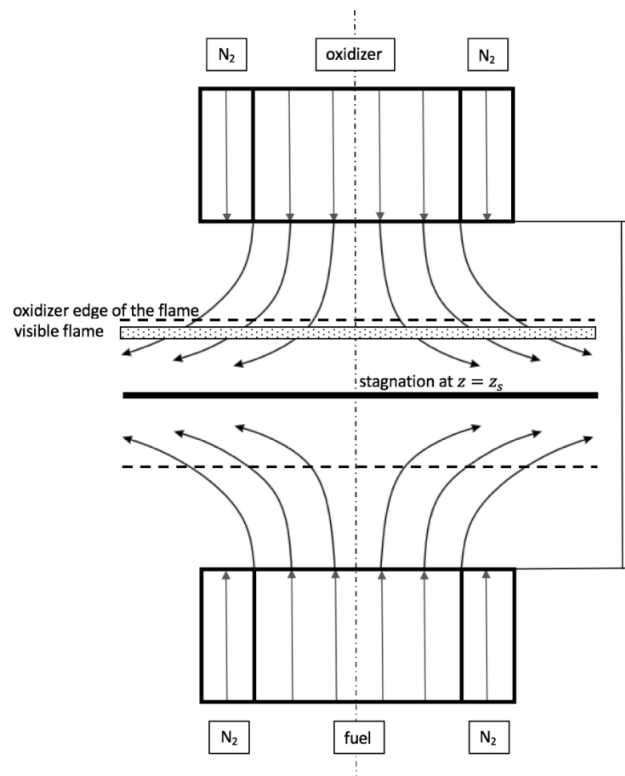


Figure 4: Schematic illustration of a counterflow flame generated by opposing nozzles. The structure of the flame consists of a reaction zone which separates a fuel rich zone and an oxidizer rich zone.

During the experiments with counter flow diffusion flames, the following three additional desirable characteristics are presumed [5]:

- The tangential components of the flow velocities at the boundaries are zero and the flow velocities along the centerline near the stagnation plane varies linearly with distance. These favorable characteristics allow to constitute the flow with the local strain rate a . The value of the strain rate is defined as the normal gradient of the normal component of the flow velocity. A detailed description and derivation of the strain rate will be exercised in chapter 2.4.2.
- The symmetry of the counterflow flame leads to planar or well-defined curvatures
- The inverse of the velocity gradient represents the characteristic flow time. By comparing the characteristic flow time to the characteristic reaction time, the Damköhler number is revealed,

$$Da = \frac{\text{Reaction rate}}{\text{Diffusion rate}} = \frac{\text{Diffusion time}}{\text{Reaction time}}. \quad (2.12)$$

In order to stabilize the flame and also to shield the reactants from the environment, curtains or also called guard flows are used. These guard flows consist of nitrogen or other inert gases and have no influence on the reaction zone. During the experiments with the counterflow burner the product gases are sucked downward into the lower part of the burner and are cooled down using water sprays which are adjusted inside the lower burner body. Furthermore, the water sprays also prevent potential flame propagation through the exhaust system.

2.4.2. Strain Rate

In counterflow configurations the strain rate is a useful tool to characterize the flow field and to quantify the velocities of the flows. The strain is defined as the normal gradient of the normal component of the flow velocity and the value changes from the fuel boundary to the oxidizer boundary. A mathematical concept for deriving the strain rate in counterflow flames was developed by Seshadri, et al. [4] [6]. To derive the equation of the strain rate a flow field which is illustrated in Figure 5 has to be considered.

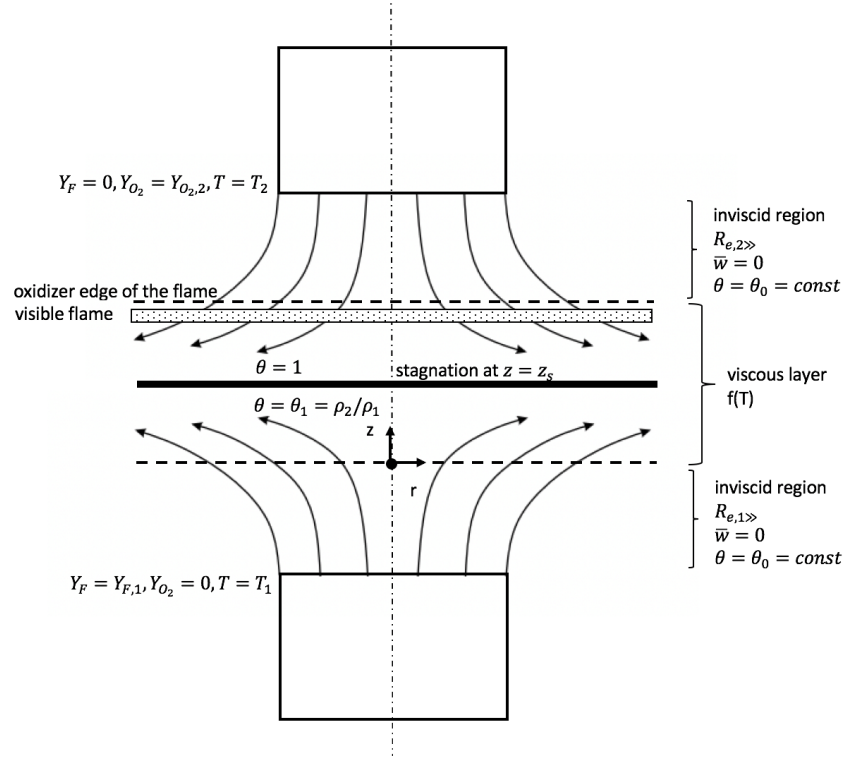


Figure 5: Schematic illustration of a laminar flowfield in a counterflow configuration

In that configuration the two flows of the two jet streams are assumed to be steady, laminar, axisymmetric, directed towards a stagnation plan and the boundaries are separated by the separation distance L . Furthermore, it has to be considered that the densities of the two flow streams are different and the flows change gradually from being uniform at the duct exits to stagnating at the stagnation surface [6]. It is also presumed that the characteristic Reynolds numbers of the flows are large so that the thin viscous viscid layer in which the reaction and the chemical reacting occurs is very small [4]. Outside the reaction zone a nonreactive and inviscid flow field is presumed. The axial coordinates z and the radial coordinate r are nondimensionalized with respect to the distance between the fuel and oxidizer duct represented by L . This separation distance is a decisive factor in the experimental performance of experiments in counterflow configurations as well as in numerical simulations. The radial component of the flow velocity u_r and the axial component of the flow velocity u_z are nondimensionalized by division by U_i . The pressure p is nondimensionalized by division by the dynamic pressure ρU_i^2 . The oxidizer duct boundary is at $z = 1$ and the fuel duct boundary is at $z = 0$. At the oxidizer duct boundary, the magnitude of the injection velocity and the temperature of the fluid at the injection plane are represented by U_2 and T_2 , respectively. At the fuel duct boundary, the magnitude of the injection

velocity and the temperature of the fluid are represented by U_1 and T_1 , respectively. The Reynold's numbers at the boundary regions are denoted by $Re,1 = U_1\rho_1L/\mu_1$ and $Re,2 = U_2\rho_2L/\mu_2$ where ρ_i, μ_i are the densities and the coefficients of viscosity, respectively. To simplify the derivation of the strain rate, it is assumed that the densities, viscosities, heat capacities and thermal conductivities are constant [6]. It follows that the radial component of the equation of motion is given by [7],

$$u_r \frac{\partial u_r}{\partial r} + u_z \frac{\partial u_r}{\partial z} = -\frac{\partial p}{\partial r} + \frac{1}{Re} \left(\frac{\partial^2 u_r}{\partial r^2} + \frac{\partial^2 u_r}{\partial z^2} \right). \quad (2.13)$$

The axial component of motion is,

$$u_r \frac{\partial u_z}{\partial r} + u_z \frac{\partial u_z}{\partial z} = -\frac{\partial p}{\partial z} + \frac{1}{Re} \left(\frac{\partial^2 u_z}{\partial r^2} + \frac{\partial^2 u_z}{\partial z^2} \right). \quad (2.14)$$

The equation for mass conservation is,

$$\frac{1}{r} \frac{\partial}{\partial r} (ru_r) + \frac{\partial u_z}{\partial z} = 0. \quad (2.15)$$

The equation for the energy conservation is given by,

$$u_r \frac{\partial \theta}{\partial r} + u_z \frac{\partial \theta}{\partial z} = \frac{1}{RePr} \left(\frac{\partial^2 \theta}{\partial r^2} + \frac{\partial^2 \theta}{\partial z^2} \right) \quad (2.16)$$

where the Prandtl number is represented by $Pr = \mu c_p/k$, respectively. By assuming large Reynolds numbers $Re \gg \infty$, both of same order [8], the previous equations simplify to,

$$u_r \frac{\partial u_r}{\partial r} + u_z \frac{\partial u_r}{\partial z} = -\frac{\partial p}{\partial r} \quad (2.17)$$

$$u_r \frac{\partial u_z}{\partial r} + u_z \frac{\partial u_z}{\partial z} = -\frac{\partial p}{\partial z} \quad (2.18)$$

$$u_r \frac{\partial \theta}{\partial r} + u_z \frac{\partial \theta}{\partial z} = 0 \quad (2.19)$$

and two inviscid regions develop on either side of the stagnation plane that is presumed to be at $z = z_s$ [4] [8]. A thin viscous layer establishes at z_s [6]. There exist solutions for which $u_r = rU(z)$ [6]. All flow quantities, except the pressure p , are functions of the axial co-ordinate only [6]. In low speed flows the radial component of the equation of motion shows that $p = P(z) - z^2Q(z)$, where Q represents a constant. This result is consistent with the equation of state for an ideal gas only at low Mach numbers [6]. All quantities used in this derivation are nondimensionalized with $T/T_2 = \rho/\rho_2 = \mu/\mu_2 = \theta(z)$ at $z = 1$. Using the equation of mass, it follows that $U/U_2 - \theta_0 f'/2 = 0$, where f represents the ratio of nondimensional axial velocity to nondimensional temperature with $f = -u_z/(\theta_0 U_2)$ and primes denote differentiation with respect to z . Thus, the radial component of the equation of motion is [6]

$$(f')^2 - 2ff'' - K/\theta_0 = 0 \quad (2.20)$$

with the constant $K = 8Q/(\rho_2 U_2^2)$. Plug flows are assumed to establish at the fuel duct boundary $z = 0$ with,

$$f' = 0, f = f_1 = -\rho_1 U_1/(\rho_2 U_2) \quad (2.21)$$

and at the oxidizer duct boundary $z = 1$ with,

$$f' = 0, f = 1 \quad (2.22)$$

Hence, the solutions to equation 2.20 which satisfies the boundary conditions in equation 2.21 and equation 2.22 are [9],

$$f = f_1 - Kz^2/(4\theta_1 f_1), \quad 0 \ll z \ll z_s \text{ and } \theta = \theta_1 = \rho_2/\rho_1 \quad (2.23)$$

$$f = 1 - K(1 - z)^2/4, \quad z_s \ll z \ll 1 \text{ and } \theta = 1. \quad (2.24)$$

The local velocity of both streams is zero at $f = 1$ and the axial component of the flow velocity is continuous across the stagnation plane. It follows from equation 2.23 and 2.24 that $K/4 = (1 - z_s)^{-2} = \theta_1 f_1^2/z_s^2$, and

$$z_s = [1 + U_2\sqrt{\rho_2}/(U_1\sqrt{\rho_1})]^{-1}. \quad (2.25)$$

Both the axial and the radial component of the flow velocity are proportional to $\theta_0 U_2 f'$ and are represented by $a = (1/L)|du_z/dz|$. The local value of a at the stagnation plane in the region $z_s < z < 1$ is obtained by using equation 2.25 and differentiating the equations 2.23 and 2.24,

$$a_2 = \frac{2U_2}{L} \left(1 + \frac{U_1\sqrt{\rho_1}}{U_2\sqrt{\rho_2}} \right). \quad (2.26)$$

The local strain rate a_2 is called the oxidizer strain rate. Furthermore, it can be shown that the local value of a at $z = z_s$ in the region $0 < z < z_s$ is given by the so-called fuel strain rate,

$$a_1 = a_2\sqrt{(\rho_2/\rho_1)}. \quad (2.27)$$

2.4.3. The S-Curve Concept

Laminar counterflow diffusion flames have in general two different burning limits, depending on different flow and boundary conditions; the point of extinction and the point of autoignition. These two phenomena can be studied from a steady-state viewpoint. That means that the relevant information to be gained is whether the system is ignitable or extinguishable, instead of analyzing the transient ignition and extinction processes [5]. To visualize these two combustion limits, the maximum reaction temperature in the reactive flow-field or the burning rates as a function of a

corresponding system Damköhler number are plotted [10] [11]. Hence, the commonly known S-shape curve, which illustrates all the possible steady chemical states that a given reacting mixture can achieve, is obtained. The S-shaped curve is characterized by two stable branches and by one unstable branch. Lower reacting flow branch of the S-curve represents the chemically frozen flow limit. In this region the reaction rates are insignificant. Along the lower branch the chemical reaction rate increases by increasing the Damköhler number and by decreasing the strain rate. A decrease in the strain rate means that the residence time of the reactants in the mixing layer is extended, which leads to higher reaction rates of reactants in the mixing layer. The ignition event occurs at $Da = Da_{ign}$, where the heat generation exceeds the heat loss in a steady state. In contrast to a reduction in the strain rate, an increase in the strain rate and a decreasing Da leads to a lower residence time of the reactants in the mixing layer and also to a decrease in the temperature. At this point not all of the chemical energy can be released during the finite residence time in the reaction layer, the flame is unable to sustain steady burning and extinguishes. [9] [5]

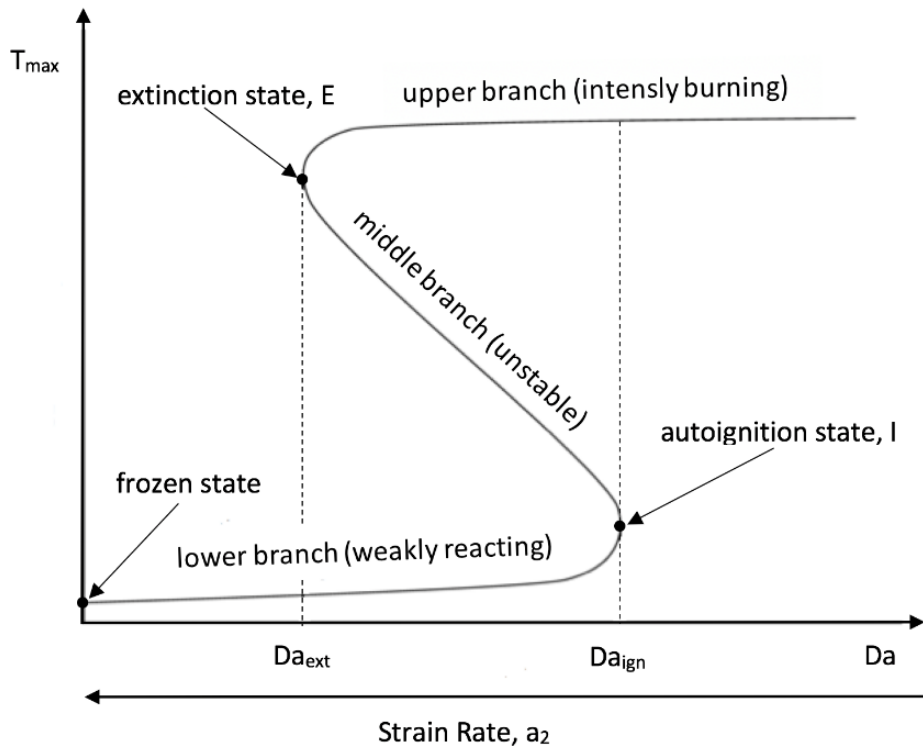


Figure 6: The maximum reaction temperature T_{max} as a function of Damköhler number – the characteristic S-curve, where Da_{ign} is the Damköhler number at ignition, and Da_{ext} is the Damköhler number at extinction.

2.4.4. Critical States of Ignition and Extinction

In combustion applications, unwanted combustion processes play a very important role in terms of both efficiency and pollutant formation. In gasoline engines for example the knocking combustion is an unwanted combustion process. To achieve high partial load efficiency today's modern gasoline engines, have a very high compression ratio. This can lead to critical conditions in the combustion chamber in the full load range, which subsequently lead to a self-autoignition event of the fuel-air mixture. In contrast to the normal combustion the so-called knocking combustion in the still unburned mixture occurs at the end of the compression process at one or more locations on a self-ignition event. As a result, the knocking combustion leads to strong pressure fluctuations in the combustion chamber which are reflected at the combustion chamber walls and lead to an increase in emissions of pollutants [2]. The second critical combustion performance factor in combustion applications is the state of extinction. The main source of unburned HC emissions in a gasoline engine is the incomplete flame spread due to extinction of the flame on the cold cylinder walls [2]. In general, low emission engines use techniques such as advanced fuel-air mixing strategies, exhaust gas recirculation and staged injection, which can be affected by flame extinction. Flame extinction is characterized by the operating conditions, local fuel/air ratio and the reaction chemistry of the fuel. [1] [2]

In computational models the causes of these two critical states can be determined with the Damköhler number for extinction Da_{ext} and for autoignition Da_{ign} .

2.4.5. Momentum Balance

To establish a stable flame midway between the two ducts in a counter flow burner a momentum balance

$$\rho_1 U_1^2 = \rho_2 U_2^2 \quad (2.28)$$

is established.

The condition of the momentum balance is very important in counter flow configurations and it also reduces heat losses from the flame to the duct. Introducing a momentum balance condition to equation 2.26 gives

$$a_2 = \frac{4U_2}{L}. \quad [9] \quad (2.29)$$

3. Apparatus and Procedure

Experimental studies are carried out to characterize the critical conditions of the autoignition and extinction event of three different pure hydrocarbon fuels by employing the counterflow configuration setup. Figure 7 is a schematic illustration of the setup. The tested liquid fuels are vaporized by using a vaporizer. The flow rates of gases are adjusted by computer-regulated mass flow controllers. All flow lines between the vaporizer and the fuel duct were heated by a heating tape to prevent condensation of fuel inside the piping and the vaporizer. A process controller controls the heating tape. The temperatures of the vaporizer exit and injection, as well as the fuel duct and the oxidizer temperature are measured with thermocouples. The flow rates of the gases are adjusted by computer-regulated mass flow controllers. The various components of the apparatus are described in the following sections.

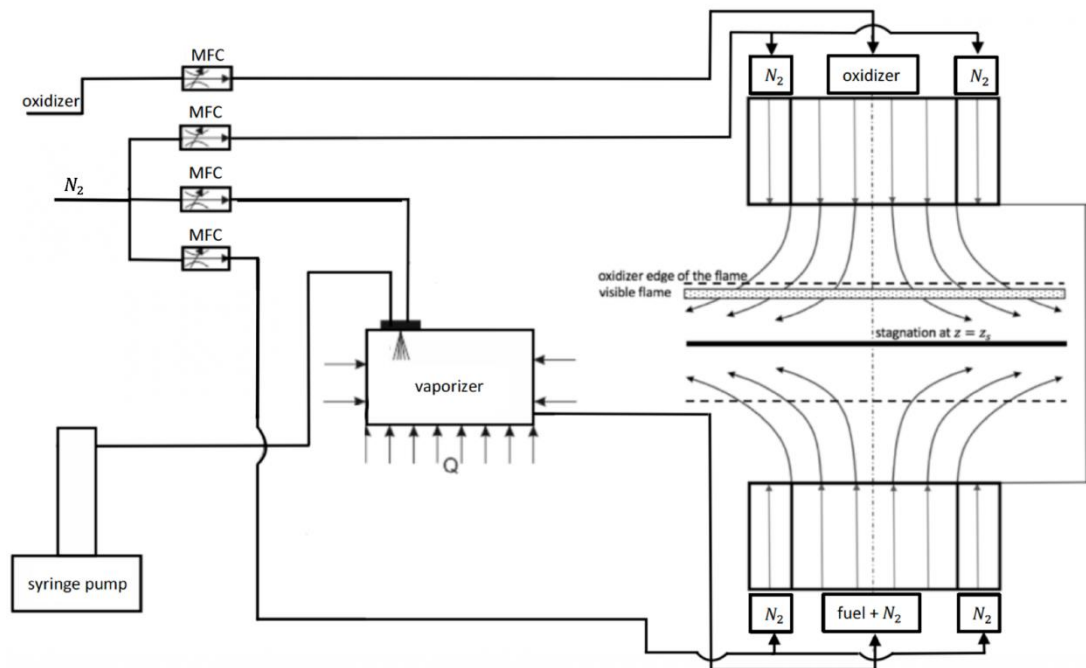
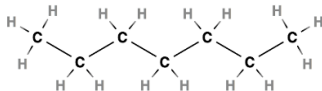
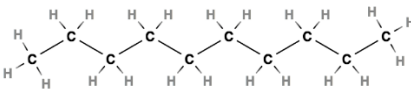
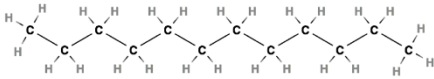


Figure 7: Schematic illustration of the experimental setup, consisting of the counterflow burner, gas and fuel supply and the mass flow controllers

3.1. Tested Fuels

Hydrocarbons consist of only carbon and hydrogen atoms and are one of the most significant classes of organic compounds. A large part of most common used fossil fuels and jet fuels consists of hydrocarbons, in particular hydrocarbons that contain between 6 and 10 carbon atoms [1]. In this thesis the combustion behavior of Alkanes, in particular n-heptane, n-decane and n-dodecane is analyzed. These pure fuels are referred to as saturated straight chain hydrocarbons and are the simplest class of their type. Saturated hydrocarbons in general consist of hydrogen and carbon atoms which are linked together with only single bonds and every carbon atom is bonded to as many hydrogen atoms as possible. The properties of the three different tested fuels can be found in Table 1.

Table 1: Properties of n-heptane, n-decane and n-dodecane [12] [13] [14]

fuel	chemical formula	molar mass [g/mol]	density at 300 K [kg/m ³]	boiling point [K]
n-heptane	C_7H_{16} 	100.2019	678.03	371.53
n-decane	$C_{10}H_{22}$ 	142.2817	725.09	447.27
n-dodecane	$C_{12}H_{26}$ 	170.3348	744.36	489.3

- n-heptane

n-heptane is a colorless liquid with a gasoline like odor and it is the major component in common used gasoline fuels. Due to its short chain length and molecular structure it burns explosively, and it sets along with pure octane the extreme ends of the octane rating scale.

- n-decane

n-decane is a colorless liquid with 22 hydrogen atoms and 10 carbon atoms. The higher number on carbon atoms lead to a higher boiling point and to a higher molecular weight compared to n-heptane. This liquid pure fuel is used in experimental studies to develop and investigate surrogates for jet fuels.

- n-dodecane

n-dodecane has the highest molecular weight of all three tested fuels and it is an oily clear liquid fuel of the paraffin series. Due to its molecular structure, it is also used as a compound in surrogates for jet fuels and in surrogates for diesel fuels.

3.2. Lower Part of the Burner

The lower part of the burner is a complex aluminum construction with the aim to guide the gaseous fuel stream into the reaction zone and to cool down the exhaust gases with water spray nozzles to prevent further reactions. The fuel stream flows through the main duct into the reaction zone. At the end of this fuel duct three stainless steel screens are placed with each separated by a stainless-steel ring. A thermocouple is placed in front of the screens on the inlet side to measure the fuel stream temperature before it enters the reaction zone. The curtain duct surrounds the fuel duct and creates co-flow jets of Nitrogen, which stabilize the fuel stream and also the oxidizer stream in the reaction zone at the borders and prevent any chemical reactions with ambient air. The exhaust gases are removed away from the reaction zone by vacuum into the internal building extraction system. Figure 8 shows a schematic section view and an image of the burner.

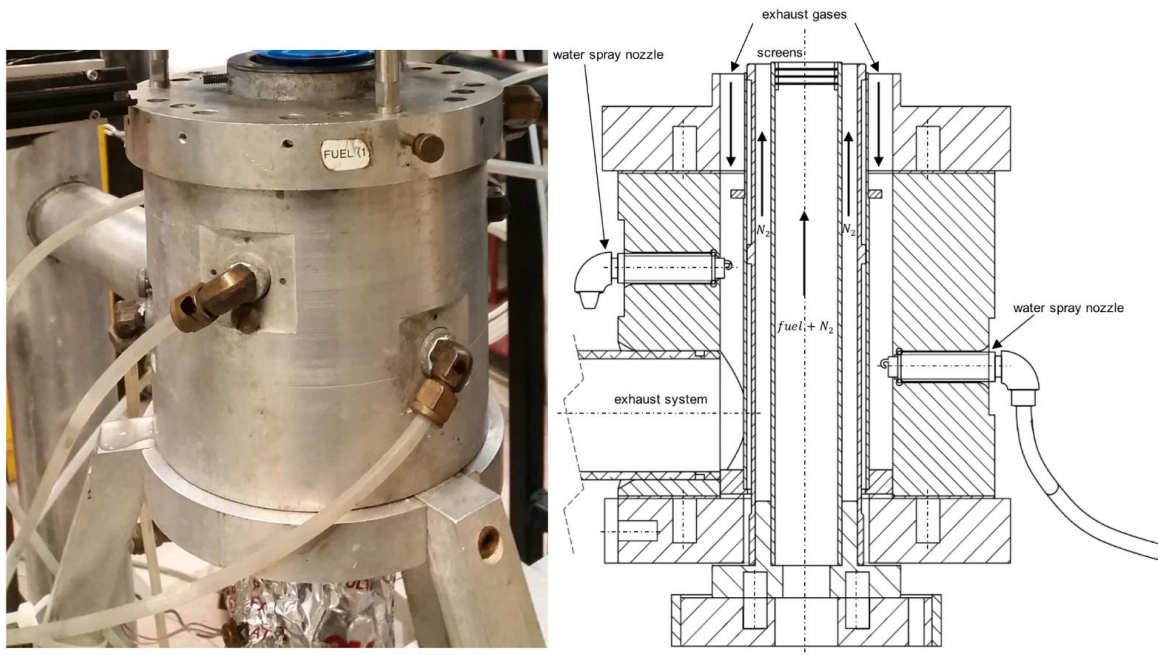


Figure 8: Schematic section view and image of the burner.

3.3. Upper Part of the Burner

The upper part of the burner or also called oxidizer duct is the most essential part of the experimental setup. It guides the oxidizer stream into the reaction zone and it also produces steady, laminar plug flow conditions which are the key points in the counterflow theory. Each top is connected to the lower part of the burner via three adjustable pins for setting the separation distance L .

For the extinction experiments a top which is illustrated in Figure 10 is used. The extinction top consists of a main duct and a surrounding annular curtain duct. The main duct guides the oxidizer stream into the reaction zone and steady laminar flow conditions with axially directed exit velocities are formed by 3 stainless steel screens at the end of the duct. All screens are held in place by 5 steel rings. These fine woven screens from Inconel have a high resistance to high temperatures and to corrosive environments. A screen and a stainless-steel ring which are used at both the autoignition top and the extinction top are shown in Figure 9.

The curtain duct with a honeycomb ring close to the end of the duct to ensure plug flow conditions guides the nitrogen curtains surround the flame to stabilize it and to shield the reactants from the environment.

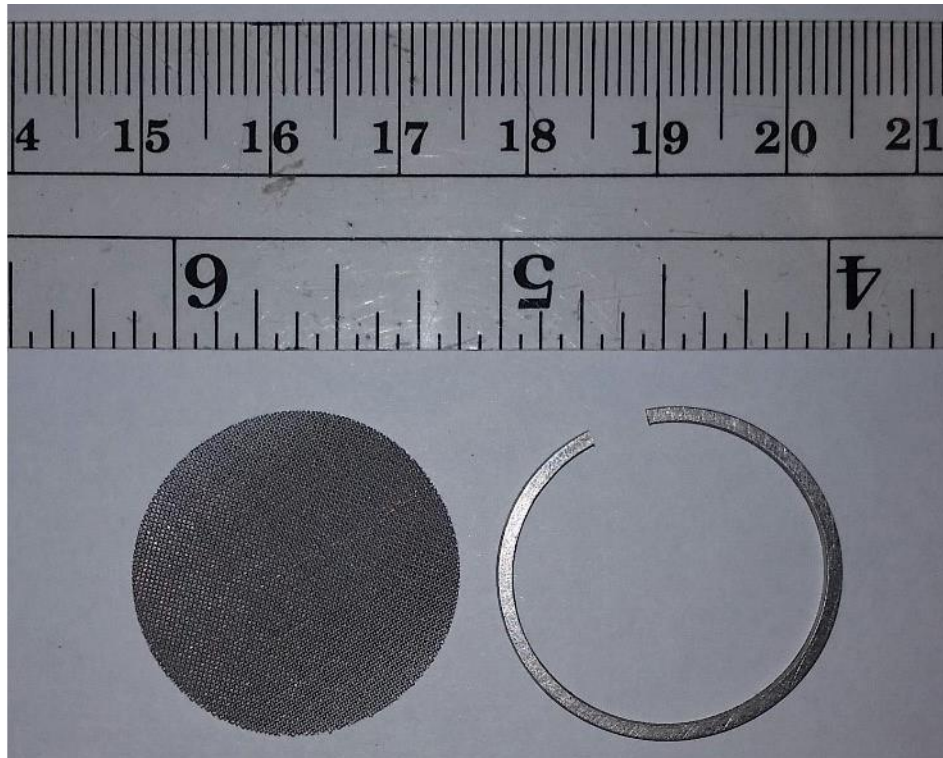


Figure 9: Inconel™ 600 gauze 200 screen woven from 0.05 mm diameter wire and an ATI 625™ nickel-based alloy stainless steel ring

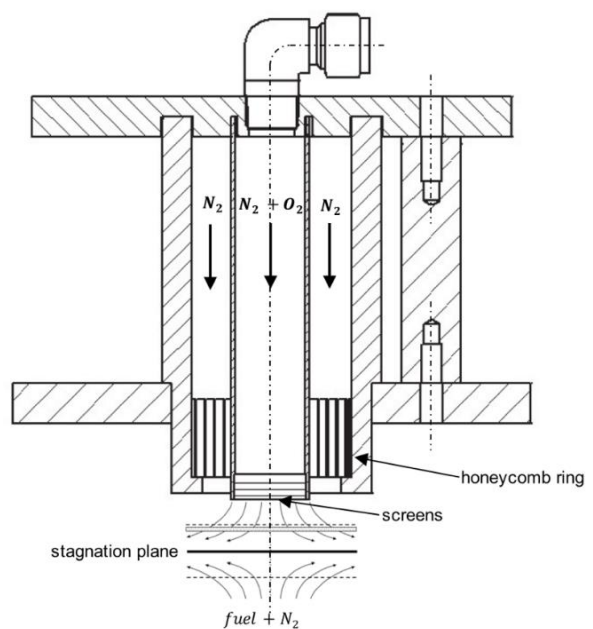
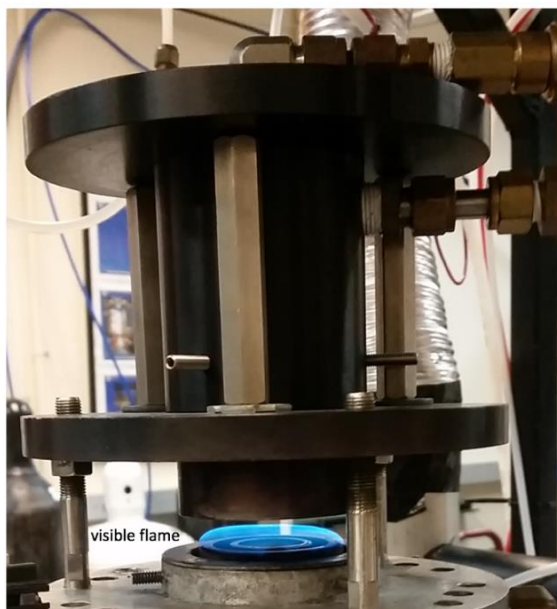


Figure 10: Schematic section view and image of the extinction top

The key features of the autoignition top are similar to that of the extinction top and the top is illustrated in Figure 11. Key part of the autoignition top is a Starbar®SER silicon carbide heating element with a central heating section referred to as a hot zone and two terminal sections called cold ends to heat up the oxidizer stream to the autoignition temperature. Temperatures of up to 1300 K degrees can be achieved with this powerful heating element. The heating element is surrounded by a quartz oxidizer duct and an annular quartz curtain duct. To prevent any damage or melting of all the non-ceramic parts the autoignition top is provided with a water-cooling system. Furthermore, the curtain duct is isolated with high-temperature Insulfrax® S Blankets. The screens used at the autoignition top are the same screens used at the extinction top and the fuel duct.

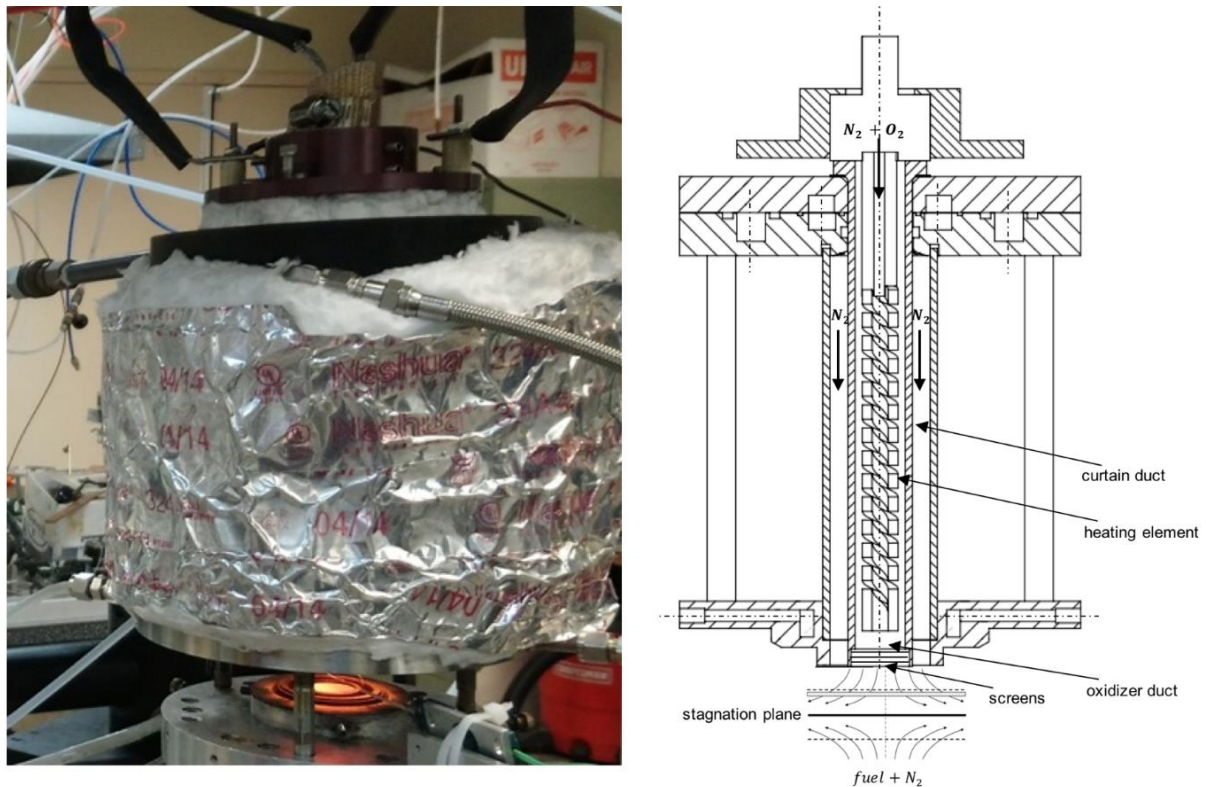


Figure 11: Schematic section view and image of the autoignition top.

3.4. Vaporizer

Extinction and autoignition experiments were carried out at atmospheric pressure using vaporized liquid fuels. A vaporizer which consists of a heated aluminium box, a BETE fog XA SR 050 fuel injection nozzle, a Bete FC07 fluid cap and a Bete AC1201 air cap is used.

The vaporizer is insulated with the same high-temperature Insulfrax® S Blankets used at the autoignition top. Vaporized fuel in the vaporizer is prevented from being ignited and burnt therein by various manners, such as leakproofness, controlling an air/fuel ratio in a range out of a combustible range and keeping vaporized fuel temperature at a level lower than its self-igniting temperature. Nitrogen is used for dilution and to carry the vaporized fuel to the burner. The temperature inside the vaporizer as well as inside the lines running from the vaporizer to the reactions zone is controlled by heating tapes and process controllers to prevent re-condensation of the vaporized fuel. The fuel injection nozzle uses the energy in compressed gas to produce highly atomized sprays at low flow rates. The nozzle is cooled by a cooling plate attached to the bottom to avoid vaporization which would influence the constant flow. The liquid fuel is supplied to the nozzle under pressure from a Teledyne Hastings 500D Syringe pump with flowrates between 0 ml/min and 15 l/min

3.5. LabView Controlling Software

To obtain most accurate and reproducible results, the entire experimental setup is controlled and monitored with a visual programming language from National Instruments, called LabVIEW. The control software uses a dataflow programming language and has been continuously improved and developed over the years. One benefit of this software is the simple monitoring, controlling and adaptation of new hardware devices such as mass flow controllers, pumps and calibration devices. For the experiments on the counterflow burner up to 5 gaseous reactants as well as one liquid reactant in each stream can be controlled. Figure 12 shows the basic control front panel of the VI during an autoignition event. The basic control front panel allows the operator to input data such as oxidizer strain rate (in the upper left), mass fractions of the fuel stream, oxidizer stream as well as of the curtains (lower right). Furthermore, this front panel allows to control the different flowrates of the streams as well as of the temperatures of the fuel stream and oxidizer stream.

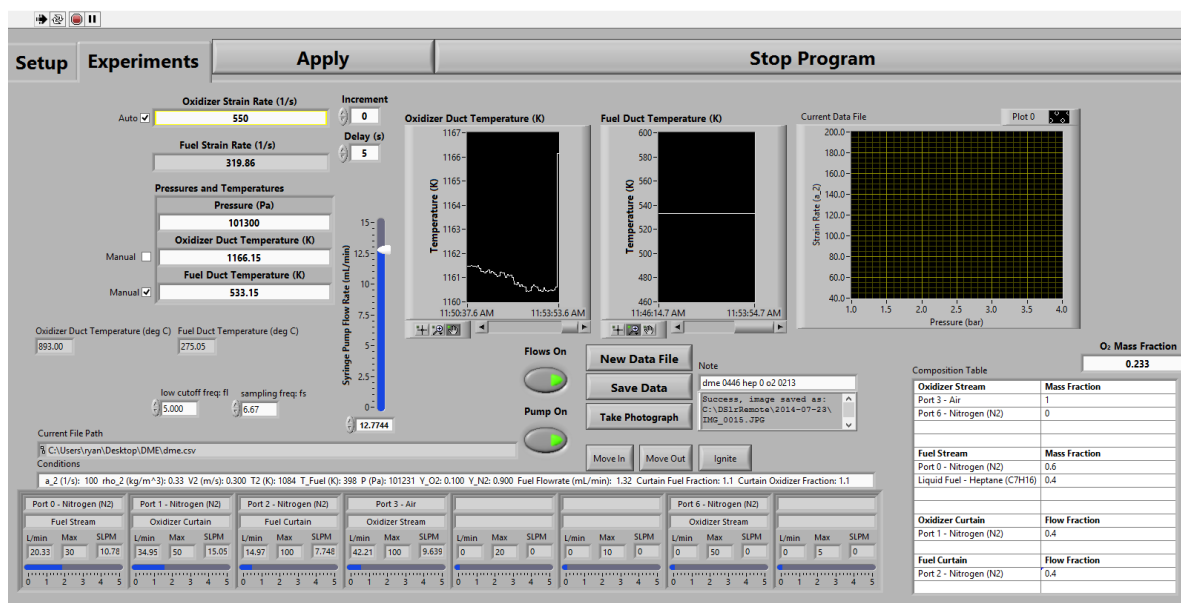


Figure 12: Basic control front panel of the counterflow software during an autoignition event

The main front panel for the software is shown in Figure 13. Before carrying out an experiment it is necessary to set up all the ports and reactant streams depending on the needed maximum flowrates as well as the type of the experiment.

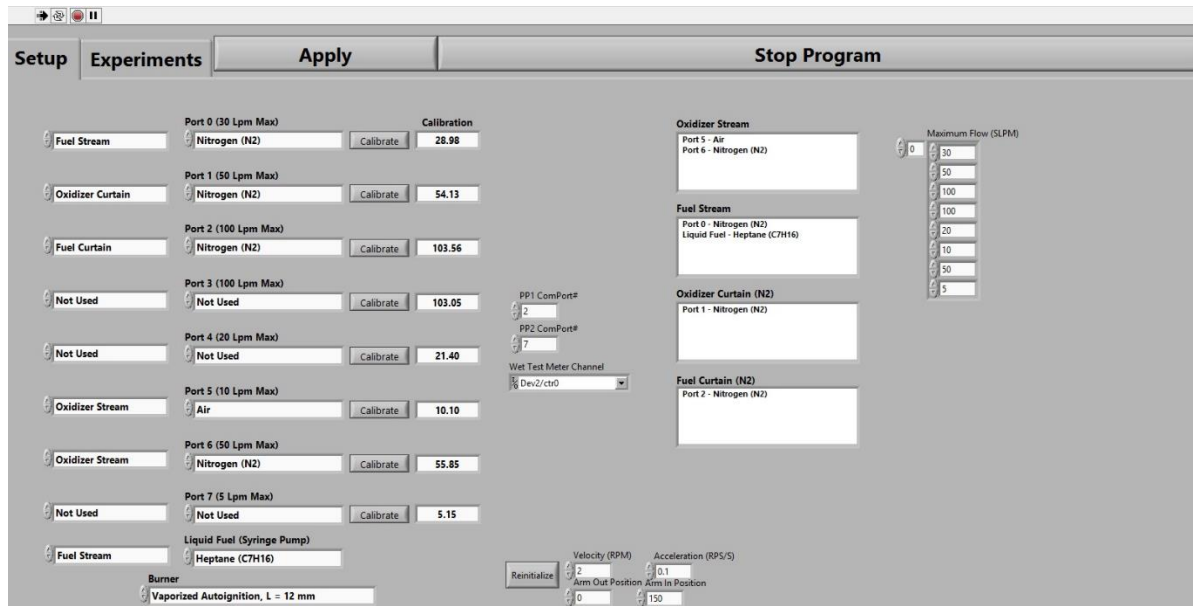


Figure 13: main front panel of the counterflow software

3.6. Gas Flow Control and Calibration

A mass flow controller is a device that automatically establishes and controls a stable flow rate of liquids or gases according to a set flow rate sent as an electric signal linear to the mass flow rate. During the experiments with the counter flow burner several Teledyne mass flow controllers are used. The controllers have flow ranges from 0-50 slm to flows of 0-100 slm and a full-scale accuracy of about 1 %. In order to obtain very accurate result, the mass flow controllers must be calibrated for the maximum flow rate in the respective working range for each individual gas needed. For the calibration of the mass flow controller a volumetric RITTER Drum-type Gas Meter with a flow range of 0.167 l/min to 33.3 l/min and a National Instruments USB-6008 device are used. The measurement device meter works on the principle of displacement and contains a revolving measuring drum within a packing liquid. The gas flowing through the meter causes a rotation of the measuring drum within the packaging fluid and the volume gets measured by periodically filling and emptying the four rigid measuring chambers. The USB device counts the pulses corresponding to the turns of the measuring drum in order to determine the volumetric flow rate. This type of gas meter is used because of the direct measurement of volumes which means that the conditions and compositions of gases have no influence on the measurement accuracy. Before each calibration, the level of the packing liquid must be checked carefully to ensure an accurate calibration. After the port of the mass flow controller is physically connected to the measurement device the calibration can be controlled using a Labview calibration routine. During the calibration the value of the maximum volumetric flowrate is directly measured, and an updated calibration value is calculated. The calibration procedure is repeated until the accuracy of the deviation of the mass flow controllers is less than $\pm 1\%$ and the standard deviation is less than $\pm 0.01\%$. Figure 14 shows the front panel of the calibration VI during the calibration procedure where the deviation of the mass flow controllers is less than $\pm 1\%$ and the standard deviation is less than $\pm 0.01\%$.

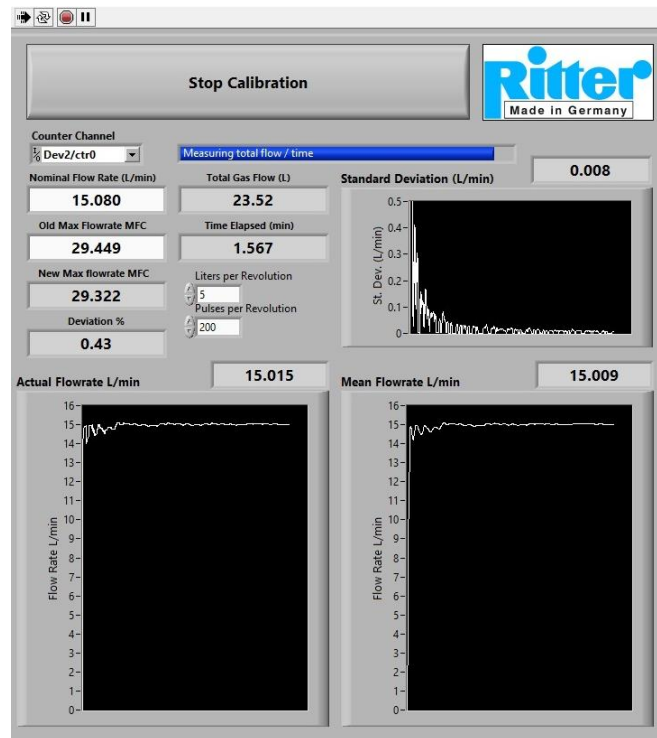


Figure 14: Front panel of the calibration VI during the calibration procedure where the deviation of the mass flow controllers is less than $\pm 1\%$ and the standard deviation is less than $\pm 0.01\%$.

3.7. Temperature Measurement and Control

Thermocouples are used for experimental diagnostics in combustion research and in high temperature processes where a quantitative knowledge of the gas temperature is required to determine appropriate kinetic rate constants and to calculate heat fluxes associated with high temperature flows. When carrying out counterflow experiments, it is necessary to know and to control the gas temperatures in the system. Especially in the pre-vaporization of a liquid fuel in the vaporizer it is important to set and control the temperatures in order to ensure complete vaporization of the liquid fuel and to prevent filling the vaporizer with the liquid fuel. After the fuel is vaporized it is also necessary to set the temperatures of the lines between the vaporizer and the burner high enough to prevent condensation of the fuel. Furthermore, the temperature of the vaporized fuel at the fuel boundary must be known for proper control of flow rates such that the gases are injected with a known temperature and velocity for later use in numerical codes. A proper and exact feedback of the conditions at the fuel ducts is necessary to control the temperature using a PID-loop process controller and also for providing real-time temperature feedback to the Labview control software. The temperatures of the fuel stream are measured with two E-type thermocouples. These

two thermocouples are placed beneath the screens on the fuel duct side. One thermocouple is connected with an Omega CN4416 temperature/process controller to control heating tapes along the flow lines. The second thermocouple is used for the so-called cold junction compensation. Therefore, the thermocouple is connected with a USB-TC module which can be used by the Labview software. Two additional E-type thermocouples are used to measure the temperatures at the vaporizer inlet and vaporizer outlet. During the autoignition experiments on the atmospheric counterflow burner a Pt/13%Rh-Pt R-type thermocouple is used to measure the oxidizer stream temperature at the oxidizer exit. This type of a thermocouple is used because of high service temperatures and stabilities. [15]

3.7.1. Temperature Correction

The most common used thermocouple in laboratory combustion applications to carry out temperature is the R-type thermocouple. To avoid any errors in the data evaluation it is very important to consider the radiation losses from the thermocouple from a high temperature gas flow to colder surroundings. Therefore, a thermocouple arrangement for combustion-system measurements with the major modes of heat transfer is desired. The energy balance for a thermocouple is given by the following equation

$$\dot{Q}_{cat} + \dot{Q}_{conv} + \dot{Q}_{rad} + \dot{Q}_{cond} = \rho c p V \frac{dT_{tc}}{dt} \quad [15]. \quad (3.1)$$

It is assumed that the thermocouple is convectively heated by the flow of a hot gas and the convective term dominates over all other terms associated with the thermocouple wire and junction [15]. In practice, the following assumptions are made to neglect the catalytic and conduction term:

- high ratio of length to diameter of the thermocouple wire (>200)
- surface-induced catalytic reactions
- small catalytic activity in an air environment

The equation of the surface-area-specific net transport, which is given by

$$\varepsilon_{tc} \sigma (T_{tc}^4 - T_w^4), \quad (3.2)$$

represents the independency of the wall emissivity with respect for exchange between a gray-emitting thermocouple surface and a much larger, isothermal enclosing diffuse-

gray surface [15]. Hence, the assumption of a steady state environment simplifies equation 3.1 to

$$h(T_g - T_{tc}) = \varepsilon_{tc}\sigma(T_{tc}^4 - T_{surr}^4). \quad (3.3)$$

For a local gas temperature equation 3.3 can be solved with

$$T_g = T_{tc} + \varepsilon_{tc}\sigma(T_{tc}^4 - T_{surr}^4)d/kNu. \quad (3.4)$$

The radiation loss of the thermocouple can then be obtained by

$$\Delta = \varepsilon_{tc}\sigma(T_{tc}^4 - T_{surr}^4)d/kNu \quad (3.5)$$

where Nu represents the Nusselt number for a cylindric problem within $0.02 < Re < 44$ with

$$Nu = (0.24 + 0.56Re_d^{0.45}) \left(\frac{T_m}{T_\infty}\right)^{17}, \text{ respectively.} \quad (3.6)$$

Here $Re = u_2d/\nu$ represents the Reynolds number with the thermocouple wire diameter d , the viscosity of the oxidizer stream ν and the oxidizer velocity $u_2 = a_2L/4$. The second right handed term in equation 3.5 is assumed to be 1. [15] [16] Table 2 shows all parameters needed for the calculation of the radiation losses of the thermocouple at an assumed air oxidizer stream temperature of 1200 [K].

Table 2: Parameter for the calculation of the radiation loss for the oxidizer stream temperature measurements with an R- type thermocouple [15] [17] [18]

T_{surr}	295.15	[K]	ambient temperature
d	0.0002	[m]	thermocouple diameter
ε	0.22		emissivity for R-type Thermocouple
σ	$5.67 * 10^{-8}$	[W/m ² K ⁴]	Stefan - Boltzmann constant
k	0.0759	[W/mK]	thermal conductivity
ρ	0.294	[kg/m ³]	density
cp	1.175	[kJ/kgK]	heat capacity
μ	0.0000465	[kg/ms]	dynamic viscosity
ν	0.00015816	[m ² /s]	kinematic viscosity

3.8. Experimental Procedure

- Autoignition at Atmospheric Pressure

The critical conditions of autoignition are measured at atmospheric pressure (1.013 bar) with vaporized liquid fuels diluted with nitrogen and an oxidizer stream consisting of oxygen and nitrogen. The temperature of the oxidizer stream at autoignition as a function of the fuel mass fraction $Y_{F,1}$ at fixed values of $Y_{O_2,2} = 0.233$, and strain rate $a_2 = 550s^{-1}$ as well as the temperature of the oxidizer stream at autoignition as a function of the mass fraction of oxygen $Y_{O_2,2}$ at fixed values of $Y_{F,1} = 0.4$, and strain rate $a_2 = 550s^{-1}$ are investigated. For each individual experiment the density at 300 K and the molecular weight of each fuel is entered into the VI. In order to obtain accurate results, the mass flow controllers are calibrated for the maximum flow rate in the respective working range for each individual gas before every experimentation. For every fuel, the experiments with fixed fuel mass fractions and various oxidizer mass fractions as well as the experiments with fixed oxidizer mass fractions and various fuel mass fractions are carried out in one day to make sure that during the experiments the same ambient conditions apply. After calibrating the mass flow controllers, the separation distance between the two ducts is set to 12 mm, the cooling system is turned on and the vaporizer and the flow lines are heated up to the defined temperature. During the heating of the vaporizer and the flowlines a constant fuel stream flow of only nitrogen prevents local overheating's of the system. The thermocouple is placed as close as possible to the screens at the end of the oxidizer duct to measure the oxidizer stream temperature at autoignition. The screens at the autoignition top are replaced after every experimentation or if any warping or damage was visible. After that the syringe pump is flushed and filled with the fuel being examined. Before heating up the autoignition top a low arbitrary strain rate is set and a flame is established with a blowtorch to control the shape of the flame and the ignitability of the mixture. The flame is held for 10 to 20 seconds to ensure that there are no residues of other fuels in the system. After that the autoignition top is heated up very slowly to avoid any thermal stress and damage. During the heating of the autoignition top a constant low oxidizer flow stream, consisting of nitrogen and oxygen, ensures an overheating of the top and it also avoids a pure nitrogen atmosphere around the Starbar heating element. Especially at high temperatures a pure nitrogen

atmosphere can result in a formation of an insulative silicon nitride layer around the heating element and to an over-temperature damage. Before reaching an estimated autoignition temperature the separation distance is checked and adjusted again because of the high heat strain of the ceramic oxidizer duct. When approaching the expected autoignition temperature all streams used are set to their defined values and the experiment can start. To investigate the oxidizer stream temperature at a certain point it is necessary to hold the temperature of the oxidizer stream at that point as constant as possible. Then the fuel pump is turned on. It is very important to maintain the fuel stream for at least 20 seconds to ensure good mixing of the reactants inside the reaction zone. If no autoignition event occurs the fuel pump is turned off and the temperature of the oxidizer stream is increased about 5 [K]. Then the procedure is repeated again until an autoignition event shown in Figure 12 occurs. After the first autoignition event occurs the oxidizer stream temperature is then decreased in steps of about 1 [K]. Every single step is examined for auto-ignition. The last point where a self-ignition of the mixture occurs is recorded and this point is repeated at least five times.

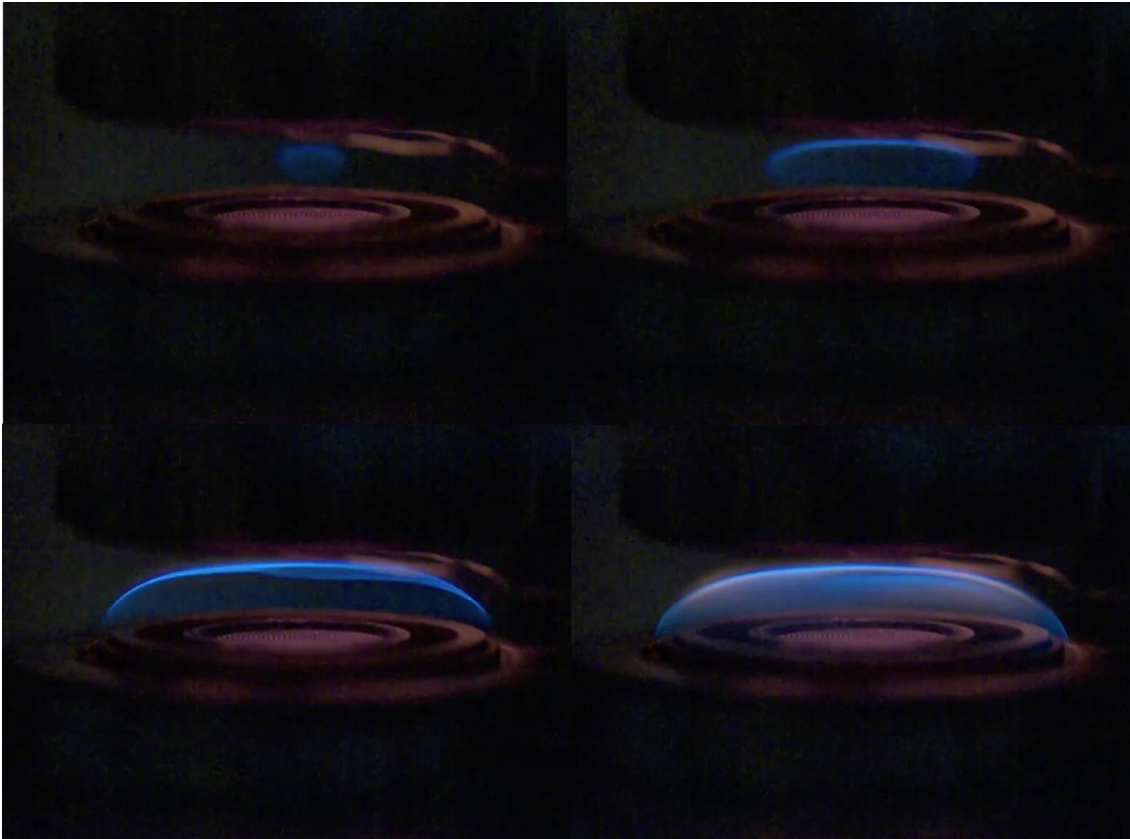


Figure 15: High speed image of an autoignition event with heptane with a fuel mass fraction of $Y_{F,1} = 0.4$, oxidizer strain rate $a_2 = 550 \text{ s}^{-1}$ and pure air as an oxidizer.

- Extinction at Atmospheric Pressure

The critical conditions of extinction are measured at an ambient pressure level of 1.013 *bar* with prevaporized liquid fuels and with fixed values of $Y_{O_2,2} = 0.233$ and various values of $Y_{F,1}$. Before starting the extinction experiments the separation distance between the two ducts is set to 10 mm and also the VI is set to the extinction setup. As same as in the autoignition experiments the cooling system is turned on and the vaporizer and the flowlines are heated up to a defined temperature and the pump is flushed and filled with the fuel being examined. During the heating of the vaporizer and the flowlines a constant fuel stream flow of only nitrogen prevents local overheating's of the system. After the defined temperatures are reached a control flame is established with a blowtorch and held for 10 to 20 seconds. To investigate a specific point, an arbitrary strain rate below the expected extinction strain rate is set and a flame is established with a blow torch. Then the oxidizer strain rate is increased at a relatively high rate of $10s^{-1}$ every 5 seconds in order to obtain a rough assessment where the flame will extinguish. As soon as the flame extinguishes a new strain rate below the first extinction strain rate is set, a new flame is established, and the oxidizer strain rate is then increased at a rate of $5s^{-1}$ every 5 seconds. The strainrate where the flame extinguishes for the second time is recorded and the mass flow controllers are calibrated for this flow rate in this working range for every gas used in the experiment. After that a strain rate close to the extinction strain rate is set and a flame is established. The strain rate is then increased with a rate of $1s^{-1}$ every 8 seconds until the flame extinguishes. This procedure is repeated at least five times for every point to be examined to obtain results as accurate as possible.

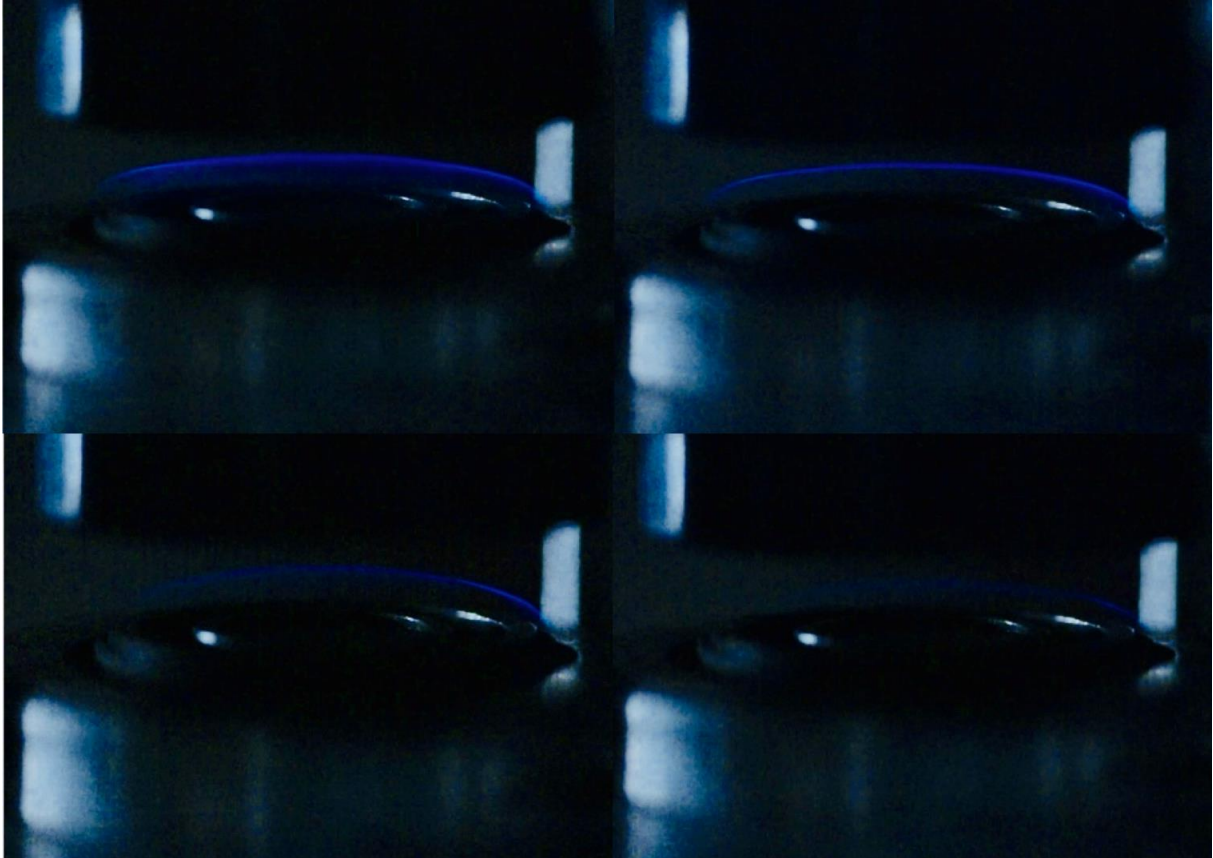


Figure 16: High speed image of an extinction event with heptane with a fuel mass fraction of $Y_{F,1} = 0.3$, oxidizer strain rate $a_2 = 345 \text{ s}^{-1}$ and pure air as an oxidizer.

4. Experimental- and Numerical Results at Atmospheric Pressure

Chapter 4 compares the experimental data and numerical predictions. Additional details of the extinction and the autoignition experiments are described in the appendix.

4.1. Results of the Autoignition Experiments

The autoignition experiments were carried out with prevaporized n-heptane, n-decane and n-dodecane at different fuel mass fractions to investigate the influence of fuel- and oxygen mass fractions on autoignition. The experiments with different fuel mass fractions were conducted from the lowest fuel mass fraction of $Y_{F,1} = 0.25$ to the highest fuel mass fraction of $Y_{F,1} = 0.5$. The experiments with different oxygen mass fractions were conducted from the lowest oxygen mass fraction of $Y_{O_2,2} = 0.07$ to the

highest oxygen mass fraction of $Y_{O_2,2} = 0.233$. The displayed experimental data points are arithmetically averaged values and all results are corrected due to radiation losses. Figure 17 shows the temperature of the oxidizer stream at autoignition, $T_{2,ign}$ as a function of the mass fraction of oxygen $Y_{O_2,2}$ for n-heptane and n-decane. The figure depicts that the autoignition temperature increases with reducing the oxygen mass fraction. Furthermore, the autoignition characteristics of n-heptane and n-decane are similar. Due to lower diffusivity of n-decane, the auto-ignition temperature is higher compared to n-heptane. In other words, lighter hydrocarbons tend to auto-ignite before heavier hydrocarbons. The difference in the autoignition temperature between both fuels at an oxygen mass fraction $Y_{O_2,2} = 0.233$ is 17.51 [K]. The difference in the autoignition temperature between both fuels at an oxygen mass fraction $Y_{O_2,2} = 0.07$ is 17.17 [K].

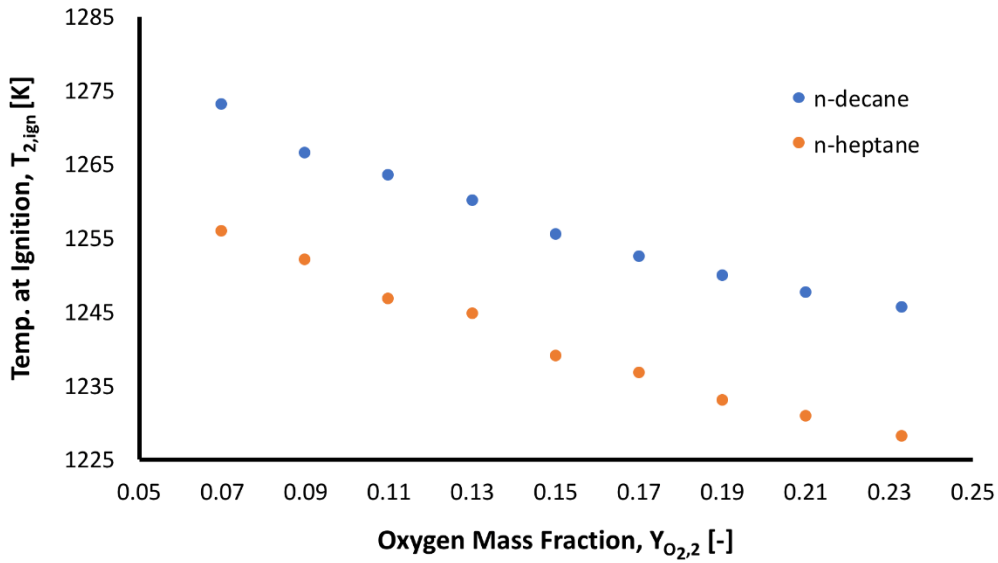


Figure 17: The temperature of the oxidizer stream at autoignition, $T_{2,ign}$ as a function of the mass fraction of oxygen $Y_{O_2,2}$ for $Y_{F,1} = 0.4$, $T_1 = 473$ [K] and $a_2 = 550$ s⁻¹.

Figure 18 shows the temperature of the oxidizer stream at autoignition, $T_{2,ign}$, as a function of the mass fraction of fuel $Y_{F,1}$ for n-heptane and n-decane. The results indicate that a variation of the fuel mass fraction has a greater influence on the autoignition temperature compared to a variation of the oxygen mass fraction. However, both experiments show a similar characteristic.

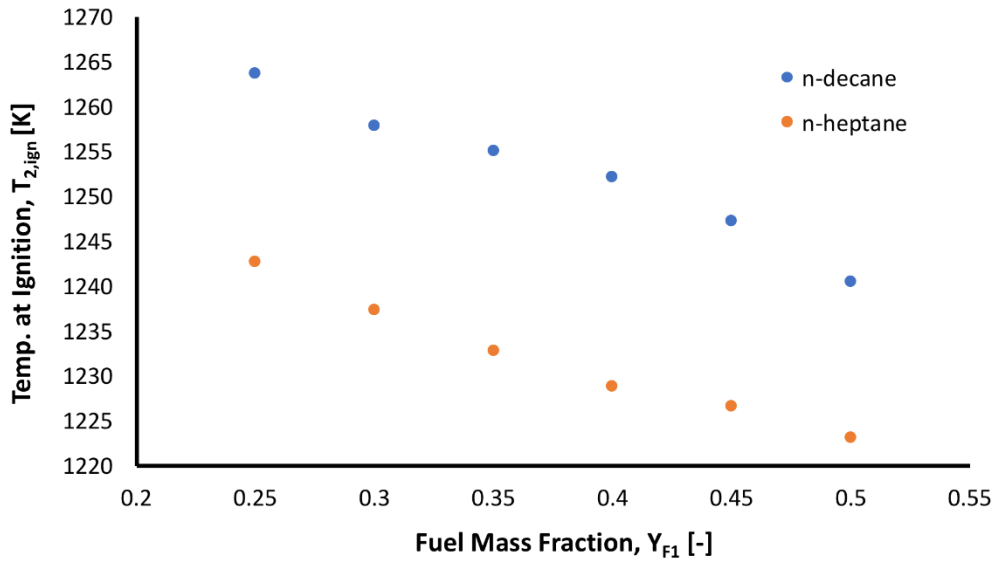


Figure 18: The temperature of the oxidizer stream at autoignition, $T_{2,ign}$ as a function of the mass fraction of fuel $Y_{F,1}$ for $Y_{O_2,2} = 0.233$, $T_1 = 473$ [K] and $a_2 = 550$ s⁻¹.

Results of the second set of experiments are shown in Figure 19 and Figure 20. In these experiments a fuel stream temperature $T_1 = 533.15$ [K] was used. The higher temperature was set because of the higher boiling point of n-dodecane, to prevent condensation of fuel inside the piping and the vaporizer. When comparing n-heptane, n-decane and n-dodecane all results show a similar characteristic. Do-decane is found to have the highest autoigniton temperatures because it has the lowest coefficient of diffusion among all tested fuels. Furthermore, the results of n-heptane and n-decane at a fuel stream temperature of $T_1 = 533.15$ [K] show a lower autoignition temperature when compared to the results in Figure 17 and Figure 18. It is anticipated that n-dodecane will also show this trend at a fuel stream temperature of $T_1 = 473.15$ [K]. Even at higher fuel stream temperatures a variation of the fuel mass fraction has a greater influence on the autoignition temperature compared to a variation of the oxygen mass fraction.

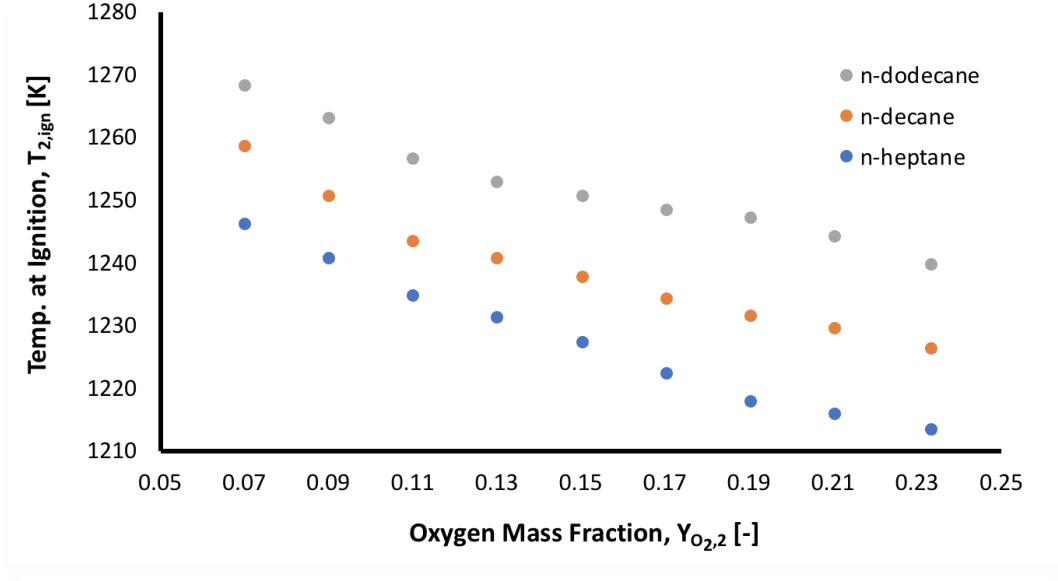


Figure 19: The temperature of the oxidizer stream at autoignition, $T_{2,ign}$ as a function of the mass fraction of oxygen $Y_{O_{2,2}}$ for $Y_{F,1} = 0.4$, $T_1 = 533.15$ [K] and $a_2 = 550$ s⁻¹.

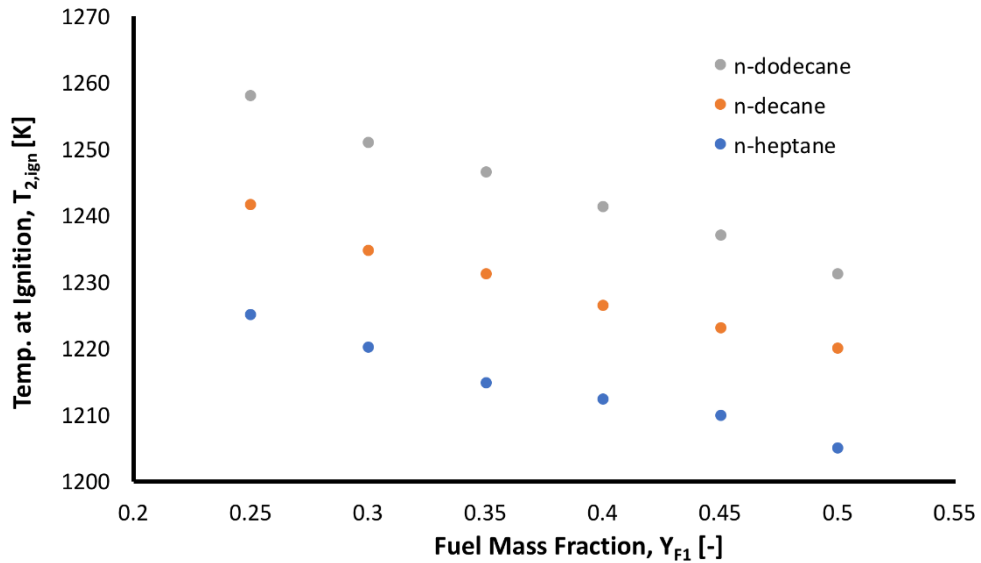


Figure 20: The temperature of the oxidizer stream at autoignition, $T_{2,ign}$ as a function of the mass fraction of fuel $Y_{F,1}$ for $Y_{O_{2,2}} = 0.233$, $T_1 = 533.15$ [K] and $a_2 = 550$ s⁻¹.

Kinetic modelling of the autoignition experiments was carried out with OpenSMOKE++ using a detailed chemical-kinematic mechanism made up of more than 13,000 elementary and lumped reactions among more than 352 species. At the fuel-boundary and oxidizer-boundary, the temperatures, T_1 and T_2 and the injection speeds of the fuel-stream v_1 , oxidizer-stream v_2 , are prescribed. For the numerical simulations plug

flow conditions were used to describe the flow field and both Soret effect and gas radiation were included in the simulations. In Figure 21 and Figure 23 the numerically calculated values of the critical conditions of autoignition of n-heptane, n-decane and n-dodecane are compared with the data obtained during the experiments. The lines represent boundaries separating a region above where autoignition takes place from a region below where autoignition cannot take place.

Figure 21 shows the temperature of the oxidizer stream at autoignition as a function of the oxygen mass fractions for all tested fuels. The experimental data show that the autoignition temperature increases with decreasing oxygen mass fraction. Whereas the calculated values of the critical conditions of autoignition for n-heptane, n-decane, and n-dodecane show that the oxygen mass fraction has no influence on the autoignition temperature and the results represent almost horizontal lines over the examined area. Hence, it was of interest to ensure that the experimental was correct and that no errors occurred, especially during the mixing of the oxidizer consisting of N_2 and O_2 . Therefore, a third experiment with n-heptane was carried out using clean compressed air as an oxidizer. The result is shown in Figure 22. The figure shows that even with pure air as an oxidizer, the trend is still the same. The little difference in the autoignition temperature between the experiments using pure air and self-mixed air as an oxidizer is assumed to be related to a new adjustment of the thermocouple.

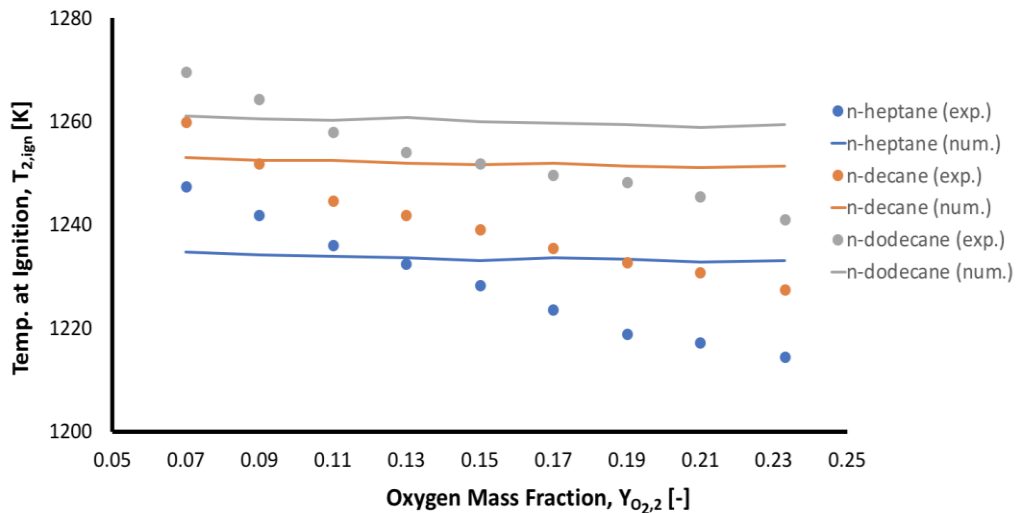


Figure 21: Comparison of the numerical calculations with the experimental results of the temperature of the oxidizer stream at autoignition $T_{2,ign}$ as a function of the mass fraction of oxygen $Y_{O_{2,2}}$ for $Y_{F,1} = 0.4$, $T_1 = 533.15$ [K] and $a_2 = 550$ s⁻¹.

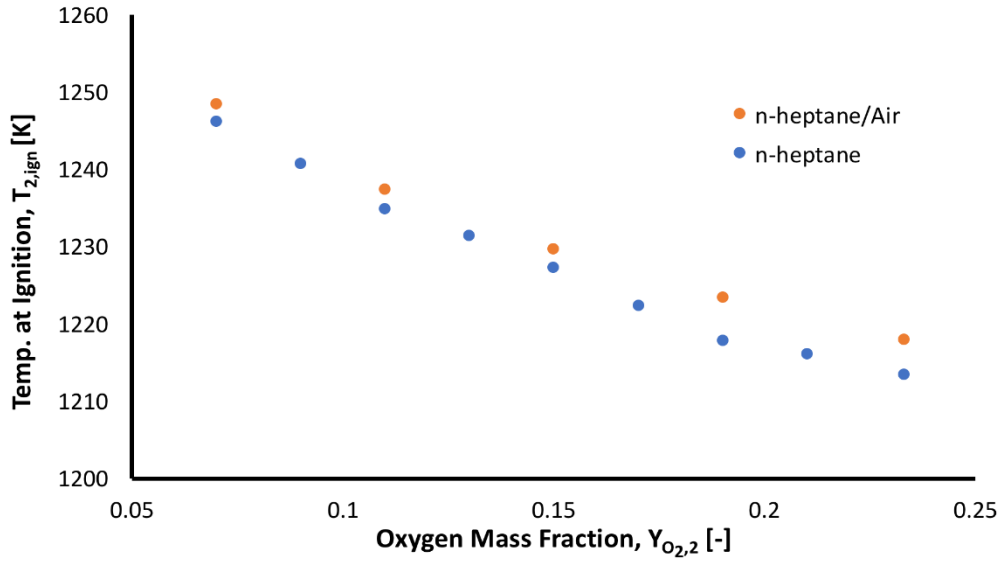


Figure 22: The temperature of the oxidizer stream at autoignition, $T_{2,ign}$ as a function of the mass fraction of oxygen $Y_{O_{2,2}}$ for $Y_{F,1} = 0.4$, $T_1 = 533.15$ [K] and $a_2 = 550$ s⁻¹.

Figure 23 shows the temperature of the oxidizer stream at autoignition as a function of the fuel mass fractions for n-heptane, n-decane and n-dodecane. The numerically calculated values of the critical conditions of autoignition agree well with experimental data. The experimental data and the calculated values of critical conditions of autoignition show that n-heptane is easiest to ignite followed by n-decane and n-dodecane. Even though the numerical data over predicts the absolute values obtained by the experimental work at all fuel mass fractions, the computational data shows the same trend.

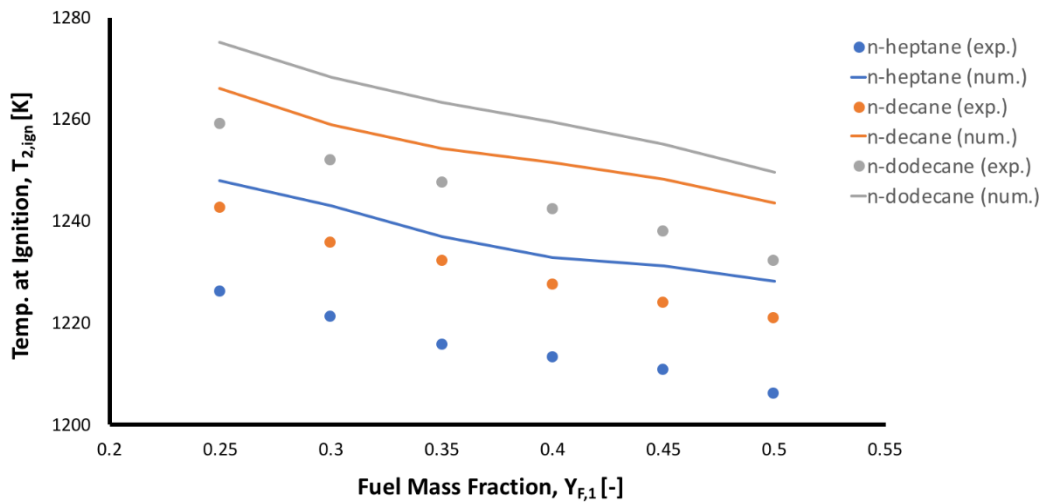


Figure 23: Comparison of the numerical calculations with the experimental results of the temperature of the oxidizer stream at autoignition $T_{2,ign}$ as a function of the mass fraction of fuel $Y_{F,1}$ for $Y_{O_{2,2}} = 0.233$, $T_1 = 533.15$ [K] and $a_2 = 550$ s⁻¹.

Figure 24 shows the fractional change in the values of the temperature at autoignition with fractional changes in the value of $Y_{O_2,2}$, $d\ln T_{2,ign}/d\ln Y_{O_2,2}$, as a function of the oxygen mass fraction $Y_{O_2,2}$. This figure was constructed using the data shown in Figure 19. Figure 25 shows the fractional change in the values of the temperature at autoignition with fractional changes in the value of $Y_{F,1}$, $d\ln T_{2,ign}/d\ln Y_{F,1}$, as a function of the oxygen mass fraction $Y_{F,1}$. This figure was constructed using the data shown in Figure 20. Both figures also indicate again that a variation of the fuel mass fraction has a greater influence on the autoignition temperature compared to a variation of the oxygen mass fraction. Of great interest is a comparison of the results from the counterflow experiments with results from shock tube experiments, where the ignition delay time τ is measured. In such experiments the ignition delay time is correlated with the following formula [19]

$$\tau = A \left[\exp \left(\frac{T_a}{T} \right) \right] \left(\frac{Y_F}{W_F} \right)^a \left(\frac{Y_{O_2}}{W_{O_2}} \right)^b W_{av}^{(a+b)} \left(\frac{p}{R} \right)^{(a+b)} \left(\frac{1}{T} \right)^{(a+b)}. \quad (4.1)$$

In this formula A is a constant, $Y_{F,1}$ is the fuel mass fraction, Y_{O_2} is the oxygen mass fraction, W_F is the molecular weight of fuel, W_{O_2} is the molecular weight of oxygen, W_{av} is the average molecular weight, p is the pressure, R is the gas constant, T the temperature, $a = 0.4$, $b = -1.20$, and $T_a = 20211.37$ [K].

This formula shows an increase in the autoignition temperature T assuming fixed τ and Y_{O_2} and a fixed fuel mass fraction Y_F . Whereas the results which were carried out in the counterflow setup show that with increasing Y_F , the autoignition temperature T decreases.

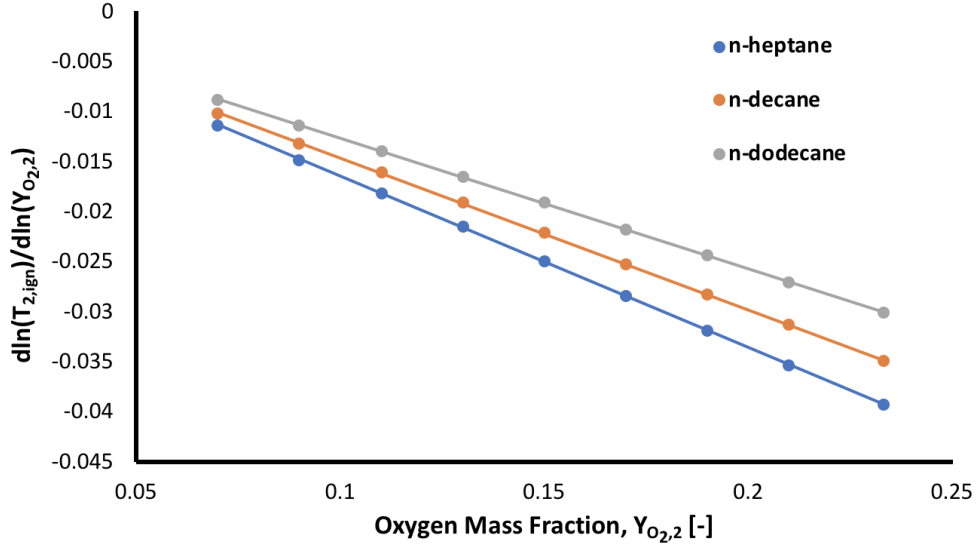


Figure 24: The fractional change in the values of the temperature at autoignition with fractional changes in the value of $Y_{O2,2}$, $d\ln T_{2,ign}/d\ln Y_{O2,2}$, as a function of the oxygen mass fraction $Y_{O2,2}$.

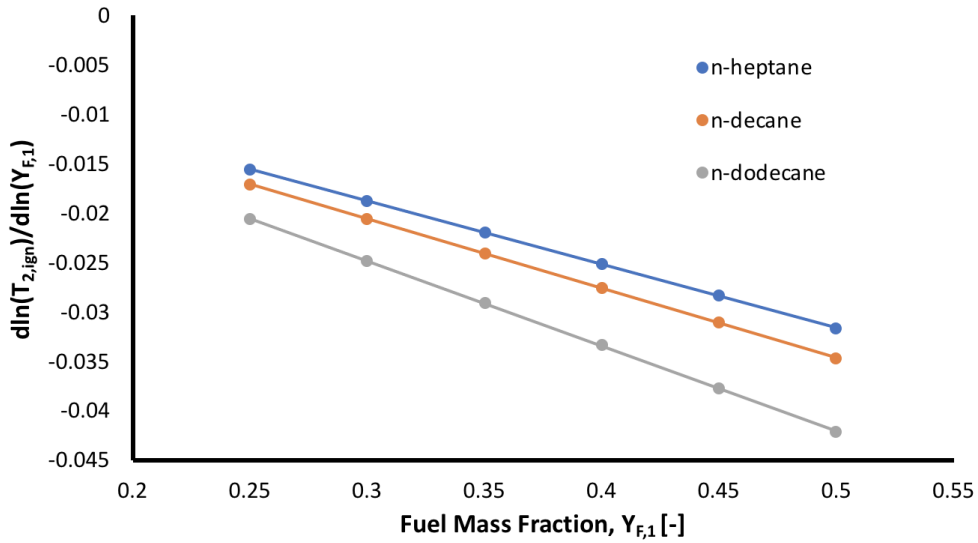


Figure 25: The fractional change in the values of the temperature at autoignition with fractional changes in the value of $Y_{F,1}$, $d\ln T_{2,ign}/d\ln Y_{F,1}$, as a function of the oxygen mass fraction $Y_{F,1}$.

4.2. Results of the Extinction Experiments

The extinction experiments were carried out to investigate the influence of different fuel mass fractions Y_F on the critical conditions of extinction. The experiments with different fuel mass fractions were conducted from the lowest fuel mass fraction of $Y_{F,1} = 0.25$ to the highest fuel mass fraction of $Y_{F,1} = 0.5$. The displayed experimental data points are arithmetically averaged values.

Figure 26 shows the experimental results of different mass fraction of fuel, $Y_{F,1}$, as a function of the strain rate at extinction, a_2 , for n-heptane, n-decane and n-dodecane. Furthermore, the results show that n-dodecane is easiest to extinguish followed by n-decane and n-heptane. This means that heavier hydrocarbons tend to extinguish easier before lighter hydrocarbons. All investigated fuels show the same trend.

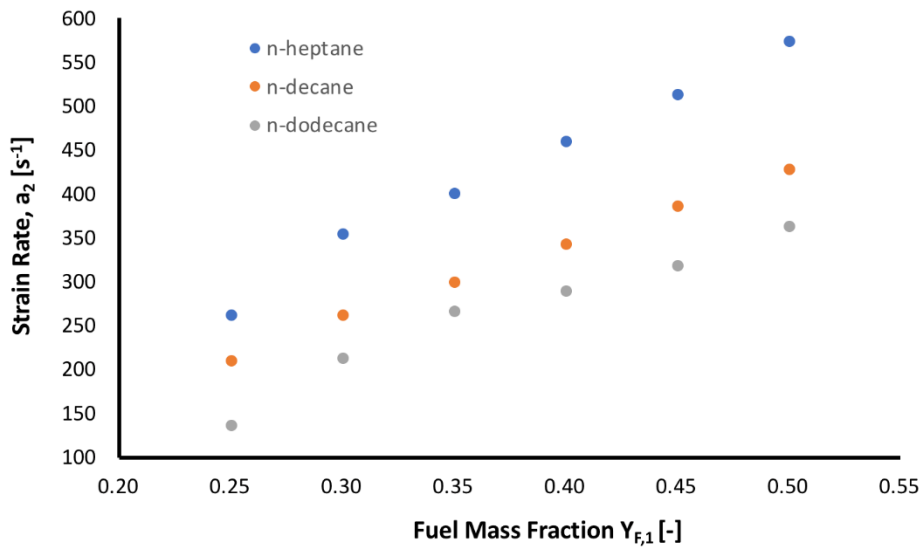


Figure 26: The extinction strain rate a_2 as a function of the mass fraction of fuel $Y_{F,1}$ for $T_1 = 533.15$ [K] and $Y_{O_2,2} = 0.233$.

Kinetic modelling of the extinction experiments was carried out with OpenSMOKE++ using two detailed chemical-kinematic mechanisms made up of more than 400 reactions among more than 100 species. For the numerical simulations plug flow conditions were used to describe the flow field and both Soret effect and gas radiation were included in the simulations. At the fuel-boundary and oxidizer-boundary, the temperatures, T_1 and T_2 and the injection speeds of the fuel-stream v_1 , oxidizer-stream v_2 , are prescribed.

The numerical predictions are compared in Figure 27 and Figure 28 with the experimental data. For the numerical calculations two different mechanism, the full and the skeletal mechanism, was used. The full mechanism includes high temperature chemistry and the skeletal mechanism includes both high and low temperature chemistry. It can be seen that the models predict the critical conditions fairly well over a wide range of different fuel mass fractions. The lines represent boundaries which separate a flammable from a nonflammable region.

In Figure 27 it can be seen that for n-heptane, the skeletal mechanism data agrees very well by the model with an average error of the same order of magnitude of the experimental uncertainty. The computational data of n-decane and n-dodecane over predict the data obtained from the experiments, but it still shows the same trend.

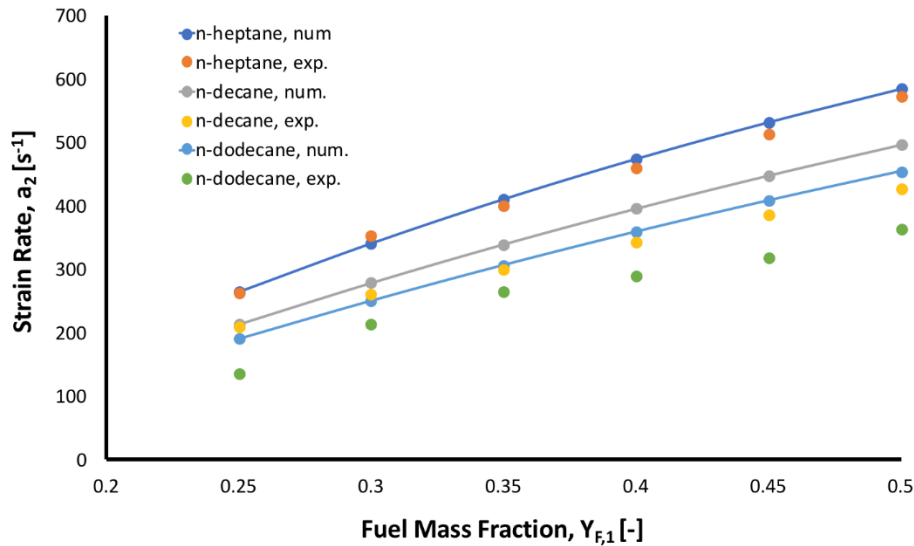


Figure 27: Comparison of the skeletal mechanism calculations with the experimental results of the extinction strain rate a_2 as a function of the mass fraction of fuel $Y_{F,1}$ for $T_1 = 533.15$ [K] and $Y_{O_2,2} = 0.233$.

Figure 28 shows that all 3 predictions improve when using a full mechanism. The average error drops from 2.7 % to 1.8 % for n-heptane, from 11.4 % to 7.0 % for n-decane and from 24.9 % to 18.1 % for n-dodecane.

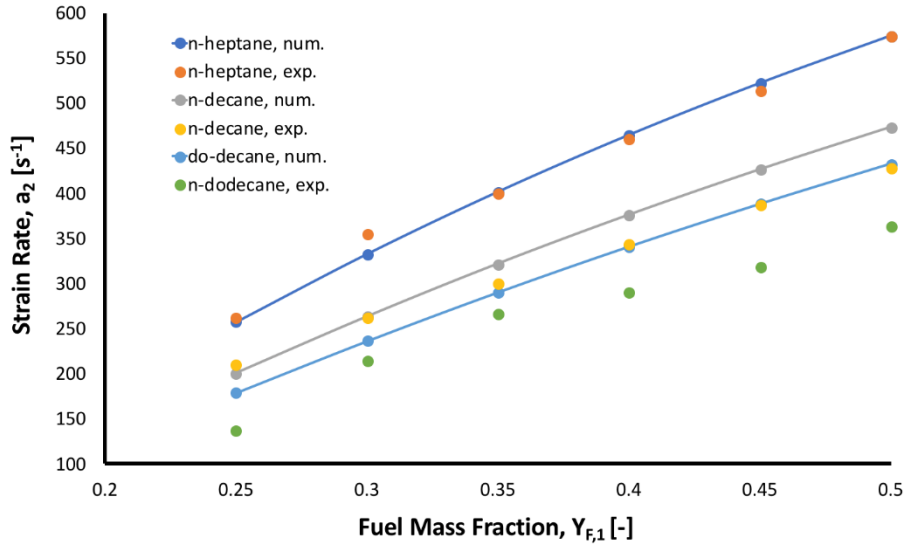


Figure 28: Comparison of the full mechanism calculations with the experimental results of the extinction strain rate a_2 as a function of the mass fraction of fuel $Y_{F,1}$ for $T_1 = 533.15$ [K] and $Y_{O_2,2} = 0.233$.

5. Autoignition of Hydrocarbon Fuels at Elevated Pressures

The objective of the following chapter is to present numerical simulations of combustion processes in elevated pressure environments. The numerical results are used to study the combustion of high molecular weight hydrocarbon fuels in a counterflow burner with laminar nonuniform flows. Developing such an understanding is important to the further development of modern combustion devices to reduce pollution emissions and increasing the efficiency. The modern gasoline engines with direct injection and turbocharging have become a key technology in recent years. Modern gasoline direct injection systems achieve a savings potential of up to 15 percent in their fuel consumption and CO_2 emissions. These gasoline engines already have a high medium-pressure level and are characterized above all by a very high level of efficiency. To achieve even greater potential based on the downsizing strategy, future engines will achieve a significantly higher-pressure level. However, this increase in the pressure level in gasoline combustion engine leads to undesirable combustion phenomena which can subsequently lead to engine damages and an increase in pollutant emissions. Many different combustion devices, such as aircraft engines, rocket engines and diesel engines, operate at pressure levels from 30 up to more than

100 bar. The influence of different fuel mass fractions $Y_{F,1}$ on autoignition at different elevated pressure levels are simulated and analyzed with the goal to help to develop advanced combustion control strategies and comprehensive understanding of combustion phenomena at elevated pressures.

5.1. Numerical Results of the Autoignition Event at Elevated Pressures

In Figure 29 the numerical results of the influence of different pressure levels on the temperature of the oxidizer stream at autoignition, $T_{2,ign}$, as a function of the mass fraction of fuel $Y_{F,1}$ for n-heptane are illustrated. The computational results show an increase of the autoignition temperature $T_{2,ign}$ by decreasing the fuel mass fraction. This is observed for all three different pressure levels and it shows the same characteristic as depicted in Figure 18, Figure 20 and Figure 22. It also can be seen that the temperature of the oxidizer stream at autoignition $T_{2,ign}$ decreases as the pressure increases.

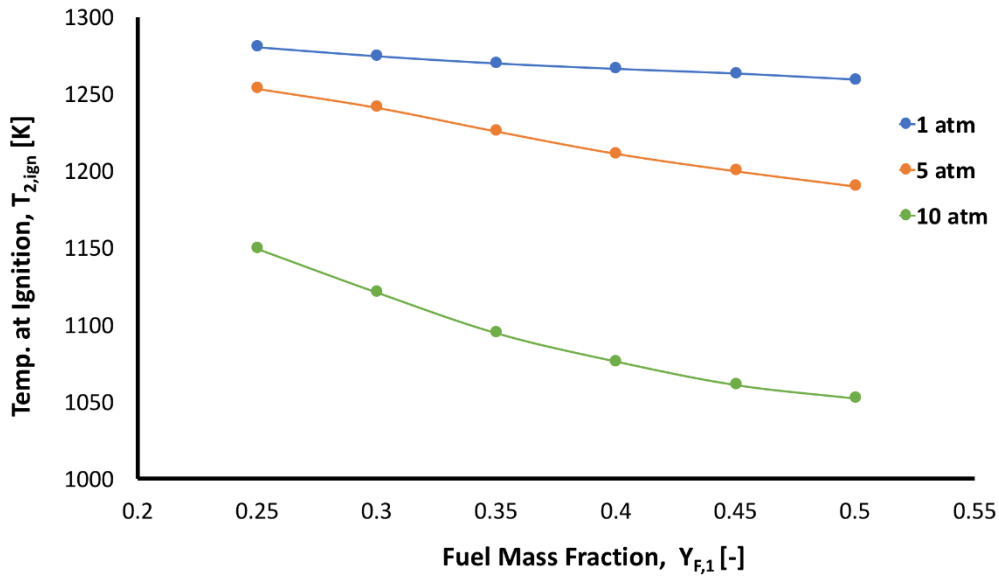


Figure 29: Numerical calculations of the temperature of the oxidizer stream at autoignition $T_{2,ign}$ at different pressure levels as a function of the mass fraction of fuel $Y_{F,1}$ for $Y_{O_2,2} = 0.233$, $T_1 = 533.15$ [K] and $a_2 = 550$ s⁻¹.

6. Concluding Remarks

The main focus of this diploma thesis was aimed to help to understand the influence of reactants on critical conditions of autoignition and extinction of high molecular hydrocarbon fuels in nonpremixed, nonuniform flows. Furthermore, numerical simulations were carried out to show the influence of different pressure levels on the temperature of the oxidizer stream at autoignition as a function of the mass fraction of fuel as well as the mass fraction of oxygen.

The experimental studies of the critical conditions of autoignition show that the autoignition temperature increases with reducing the oxygen mass fraction. Furthermore, the autoignition characteristics of the tested fuels show a similar characteristic even at different fuel stream temperatures and it can also be shown that the autoignition temperature decreases by increasing the fuel stream temperature and of all tested fuels n-dodecane showed the highest autoignition temperature. Since the numerical simulations show almost no influence on the oxygen content on the autoignition temperature, further improvement of the mechanism is necessary. The results also show that a variation of the fuel mass fraction has a greater influence on the autoignition temperature compared to a variation of the oxygen mass fraction, but they still show the same characteristic. The experimental results of the reference fuels were analyzed and found to be in general agreement with the predictions of kinetic models conducted by Modeling Group of Politecnico di Milano. The computational results at different elevated pressures show an increase of the autoignition temperature $T_{2,ign}$ by decreasing the fuel mass fraction. This is observed for all three different pressure levels. It also can be seen that the temperature of the oxidizer stream at autoignition decreases as the pressure increases.

During the extinction experiments it was found that the extinction strain rate increases almost linear with increasing the fuel mass fraction. Two different numerical mechanisms were performed, and both match the experiments very well.

References

- [1] G. P. Merker and C. Schwarz, Combustion Engines Development - Mixture Formation, Combustion, Emissions and Simulation, Berlin: Springer, ISBN: 978-3-642-02951-6, 2012.
- [2] R. van Basshuysen, Handbuch Verbrennungsmotor - Grundlagen, Komponenten, Systeme, Perspektiven, Berlin: Springer, ISBN: 978-3-658-04677-4, 2014.
- [3] C. Mortimer, Chemie - Basiswissen der Chemie, Stuttgart: Thieme, ISBN: 3134843072, 2001, 2001.
- [4] R. Seiser, K. Seshadri, E. Piskernik and A. Linan, Ignition in the Viscous Layer Between Counterflowing Streams - Asymptotic Theory with Comparison to Experiments, Department of Mechanical and Aerospace Engineering at University of California at San Diego, Departamento de Motopropulsión y Termofluidodinámica Universidad Politécnica de Madrid, 2000.
- [5] J. Warnatz, U. Maas and R. W. Dibble, Combustion - Physical and Chemical Fundamentals, Modeling and Simulation, Experiments, Pollutant Formation, Berlin Heidelberg: Springer, ISBN: 978-3-540-25992-3, 2006.
- [6] K. Seshadri and F. A. Williams, Laminar Flow between parallel Plates with Injection of a Reactant at high Reynolds Number, International Journal of Heat and Mass Transfer, 21(2):251–253, 1978.
- [7] B. R. Bird, W. E. Stewart and E. N. Lightfoot, Transport Phenomena, New York: John Wiley & Sons, ISBN: 0-471-41077-2, 2002.
- [8] U. Niemann, K. Seshadri and F. A. Williams, "sciencedirect," 09 December 2014. [Online]. Available: https://ac.els-cdn.com/S0010218014003757/1-s2.0-S0010218014003757-main.pdf?_tid=50611f7a-e907-4c41-97eb-9cebdd13304a&acdnat=1523656973_403d566e9410265bb082e16b2603b2a3. [Accessed 13 April 2018].
- [9] R. Gehmlich, Experimental Studies on Nonpremixed Combustion at Atmospheric and Elevated Pressures, Dissertation, University of California, San Diego, 2015.
- [10] A. Linan, The asymptotic structure of counterflow diffusion flames for large activation energies, Acta Astronautica, 1(7-8):1007–1039, 1974.
- [11] F. E. Fendell, Ignition and extinction in combustion of initially unmixed reactants, Journal of Fluid Mechanics, 21(2):291–303, 1965.
- [12] "NIST Chemistry WebBook, SRD 69," 2017. [Online]. Available: <https://webbook.nist.gov/cgi/cbook.cgi?ID=142-82-5>. [Accessed 01 01 2018].
- [13] "NIST Chemistry WebBook, SRD 69," 2017. [Online]. Available: <https://webbook.nist.gov/cgi/cbook.cgi?ID=124-18-5>. [Accessed 01 01 2018].
- [14] "NIST Chemistry WebBook, SRD 69," 2017. [Online]. Available: <https://webbook.nist.gov/cgi/cbook.cgi?ID=C112403&Mask=200>. [Accessed 01 01 2018].
- [15] C. R. Shaddix, "Correcting Thermocouple Measurements for Radiation Loss - a critical Review," in *Proceedings of the 33rd National Heat Transfer Conference*, Livermore, 1999.
- [16] I. L. Roberts, J. E. Coney and B. M. Gibbs, "schienedirect," 12 March 2012. [Online]. Available: https://ac.els-cdn.com/S1359431111001529/1-s2.0-S1359431111001529-main.pdf?_tid=9aec1925-1237-44f3-8e9a-

63453d177daf&acdnat=1524529470_b746e9b20c24c0167b73589deab7d131.
[Accessed 23 April 2018].

- [17] "Neutrium," 24 August 2012. [Online]. Available:
<https://neutrium.net/properties/properties-of-air/>. [Accessed 07 February 2018].
- [18] "Thermopedia," 2011 February 2011. [Online]. Available:
<http://www.thermopedia.com/fr/content/553/>. [Accessed 07 February 2018].
- [19] M. B. Colket and L. J. Spadaccini, "Journal of Propulsion and Power, 17 (2001) 315–323.," *Journal of Propulsion and Power*, vol. 17, pp. 315-323, 2001.
- [20] G. Dusan and D. Gruden, *Umweltschutz in der Automobilindustrie - Motor, Kraftstoffe Recycling*, Wießbaden: Vieweg+Teubner, ISBN: 978-3-8348-0404-4, 2008, 2008.
- [21] G. Merker, C. Schwarz, G. Stiesch and F. Otto, *Verbrennungsmotoren - Simulation der Verbrennung und Schadstoffbildung*, Wiesbaden: Vieweg+Teubner Verlag, ISBN: 978-3-8351-9069-6, 2006.
- [22] C. K. Law, *Combustion Physics*, Cambridge: Cambridge University Press, ISBN: 9780511754517, 2010.
- [23] M. Kieberger, *Untersuchung des Phänomens der Vorentflammung bei der ottomotorischen Verbrennung zur Bestimmung von Einflussfaktoren von Auslösemechanismen*, Dissertation at Institute for Powertrains and Automotive Technology Vienna University of Technology, 2012.
- [24] J. Jarosinski and B. Veyssiere, *Combustion Phenomena - Selected Mechanism of Flame Propagation, and Extinction*, Taylor & Francis Group, ISBN: 978-0-8493-8409-7, 2009.
- [25] K. A. Connors, *Chemical Kinetics - The Study of Reaction Rates in Solution*, New York: John Wiley & Sons, ISBN: 978-0471720201, 1990.

Figures

Figure 1: Diagram of the hydrocarbon oxidation process [1].....	2
Figure 2: Schematic figure of the chemical bond energy as a function of the reaction coordinate	4
Figure 3: H ₂ -O ₂ explosion diagram	6
Figure 4: Schematic illustration of a counterflow flame generated by opposing nozzles. The structure of the flame consists of a reaction zone which separates a fuel rich zone and an oxidizer rich zone.	7
Figure 5: Schematic illustration of a laminar flowfield in a counterflow configuration ..	9
Figure 6: The maximum reaction temperature T_{\max} as a function of Damköhler number – the characteristic S-curve, where Da_{ign} is the Damköhler number at ignition, and Da_{ext} is the Damköhler number at extinction.	12
Figure 7: Schematic illustration of the experimental setup, consisting of the counterflow burner, gas and fuel supply and the mass flow controllers	14
Figure 8: Schematic section view and image of the burner.....	17
Figure 9: Inconel™ 600 gauze 200 screen woven from 0.05 mm diameter wire and an ATI 625™ nickel-based alloy stainless steel ring	18
Figure 10: Schematic section view and image of the extinction top.....	18
Figure 11: Schematic section view and image of the autoignition top.....	19
Figure 12: Basic control front panel of the counterflow software during an autoignition event.....	21
Figure 13: main front panel of the counterflow software	21
Figure 14: Front panel of the calibration VI during the calibration procedure where the deviation of the mass flow controllers is less than $\pm 1\%$ and the standard deviation is less than $\pm 0.01\%$	23
Figure 15: High speed image of an autoignition event with heptane with a fuel mass fraction of $YF, 1 = 0.4$, oxidizer strain rate $a_2 = 550 \text{ s}^{-1}$ and pure air as an oxidizer.	27
Figure 16: High speed image of an extinction event with heptane with a fuel mass fraction of $YF, 1 = 0.3$, oxidizer strain rate $a_2 = 345 \text{ s}^{-1}$ and pure air as an oxidizer.	29

Figure 17: The temperature of the oxidizer stream at autoignition, $T_{2,ign}$ as a function of the mass fraction of oxygen $Y_{O2,2}$ for $Y_{F,1} = 0.4$, $T_1 = 473 [K]$ and $a_2 = 550 s - 1$	30
Figure 18: The temperature of the oxidizer stream at autoignition, $T_{2,ign}$ as a function of the mass fraction of fuel $Y_{F,1}$ for $Y_{O2,2} = 0.233$, $T_1 = 473 [K]$ and $a_2 = 550 s - 1$	31
Figure 19: The temperature of the oxidizer stream at autoignition, $T_{2,ign}$ as a function of the mass fraction of oxygen $Y_{O2,2}$ for $Y_{F,1} = 0.4$, $T_1 = 533.15 [K]$ and $a_2 = 550 s - 1$	32
Figure 20: The temperature of the oxidizer stream at autoignition, $T_{2,ign}$ as a function of the mass fraction of fuel $Y_{F,1}$ for $Y_{O2,2} = 0.233$, $T_1 = 533.15 [K]$ and $a_2 = 550 s - 1$	32
Figure 21: Comparison of the numerical calculations with the experimental results of the temperature of the oxidizer stream at autoignition $T_{2,ign}$ as a function of the mass fraction of oxygen $Y_{O2,2}$ for $Y_{F,1} = 0.4$, $T_1 = 533.15 [K]$ and $a_2 = 550 s - 1$	33
Figure 22: The temperature of the oxidizer stream at autoignition, $T_{2,ign}$ as a function of the mass fraction of oxygen $Y_{O2,2}$ for $Y_{F,1} = 0.4$, $T_1 = 533.15 [K]$ and $a_2 = 550 s - 1$	34
Figure 23: Comparison of the numerical calculations with the experimental results of the temperature of the oxidizer stream at autoignition $T_{2,ign}$ as a function of the mass fraction of fuel $Y_{F,1}$ for $Y_{O2,2} = 0.233$, $T_1 = 533.15 [K]$ and $a_2 = 550 s - 1$	34
Figure 24: The fractional change in the values of the temperature at autoignition with fractional changes in the value of $Y_{O2,2}$, $dlnT_{2,ign}/dlnY_{O2,2}$, as a function of the oxygen mass fraction $Y_{O2,2}$	36
Figure 25: The fractional change in the values of the temperature at autoignition with fractional changes in the value of $Y_{F,1}$, $dlnT_{2,ign}/dlnY_{F,1}$, as a function of the oxygen mass fraction $Y_{F,1}$	36
Figure 26: The extinction strain rate a_2 as a function of the mass fraction of fuel $Y_{F,1}$ for $T_1 = 533.15 [K]$ and $Y_{O2,2} = 0.233$	37

Figure 27: Comparison of the skeletal mechanism calculations with the experimental results of the extinction strain rate a_2 as a function of the mass fraction of fuel $Y_{F,1}$ for $T_1 = 533.15 [K]$ and $Y_{O_2,2} = 0.233$	38
Figure 28: Comparison of the full mechanism calculations with the experimental results of the extinction strain rate a_2 as a function of the mass fraction of fuel $Y_{F,1}$ for $T_1 = 533.15 [K]$ and $Y_{O_2,2} = 0.233$	39
Figure 29: Numerical calculations of the temperature of the oxidizer stream at autoignition $T_{2,ign}$ at different pressure levels as a function of the mass fraction of fuel $Y_{F,1}$ for $Y_{O_2,2} = 0.233$, $T_1 = 533.15 [K]$ and $a_2 = 550 s^{-1}$	40

APPENDIX

Extinction

- n-heptane

$Y_{O_2,2}$	0.233	0.233	0.233	0.233	0.233	0.233	0.233	0.233	0.233
Fuel Flow Rate (mL/min)	29.21	22.82	22.77	22.90	22.86	22.99	17.75	17.79	
P (Pa)	101300	101300	101300	101300	101300	101300	101300	101300	101300
T_1 (K)	533.15	533.15	533.15	533.15	533.15	533.15	533.15	533.15	533.15
T_2 (K)	295.15	295.15	295.15	295.15	295.15	295.15	295.15	295.15	295.15
v_1 (m/s)	1.56	1.43	1.43	1.44	1.44	1.44	1.32	1.33	
v_2 (m/s)	1.43	1.28	1.27	1.28	1.28	1.29	1,15	1.15	
ρ_1 (kg/m^3)	100.06	94.73	94.73	94.73	94.73	94.73	89.93	89.93	
ρ_2 (kg/m^3)	119.08	119.08	119.08	119.08	119.08	119.08	119.08	119.08	
a_1 (1/s)	626.19	574.06	572.94	576.31	575.19	578.55	529.33	530.48	
a_2 (1/s)	574	512	511	514	513	517	461	462	
$Y_{F,1}$	0.5	0.45					0.4		

0.233	0.233	0.233	0.233	0.233	0.233	0.233	0.233	0.233	0.233	0.233	0.233	0.233
17.75	17.79	17.75	17.72	13.17	13.17	13.17	13.21	13.21	9.79	9.74	9.74	
101300	101300	101300	101300	101300	101300	101300	101300	101300	101300	101300	101300	101300
533.15	533.15	533.15	533.15	533.15	533.15	533.15	533.15	533.15	533.15	533.15	533.15	533.15
295.15	295.15	295.15	295.15	295.15	295.15	295.15	295.15	295.15	295.15	295.15	295.15	295.15
1.32	1.33	1.32	1.32	1.18	1.18	1.18	1.18	1.18	1.07	1.06	1.06	
1.15	1.15	1.15	1.14	1	1	1	1	1	0.89	0.88	0.88	
89.93	89.93	89.93	89.93	85.60	85.60	85.60	85.60	85.60	81.67	81.67	81.67	
119.08	119.08	119.08	119.08	119.08	119.08	119.08	119.08	119.08	119.08	119.08	119.08	
529.33	530.48	529.33	528.18	471.79	471.79	471.79	472.97	472.97	428.68	426.26	426.26	
460	461	460	460	400	401	400	401	401	355	354	353	
				0.35					0.3			

0.233	0.233	0.233	0.233	0.233	0.233	0.233	0.233	0.233	0.233
9.82	9.79	9.82	5.89	5.87	6.00	5.89	5.87	5.89	5.89
101300	101300	101300	101300	101300	101300	101300	101300	101300	101300
533.15	533.15	533.15	533.15	533.15	533.15	533.15	533.15	533.15	533.15
295.15	295.15	295.15	295.15	295.15	295.15	295.15	295.15	295.15	295.15
1.07	1.07	1.07	0.81	0,81	0,82	0,81	0,81	0,81	0,81
0.89	0.89	0.89	0.65	0.65	0.67	0.65	0.65	0.65	0.65
81.67	81.67	81.67	78.08	78.08	78.08	78.08	78.08	78.08	78.08
119.08	119.08	119.08	119.08	119.08	119.08	119.08	119.08	119.08	119.08
429.88	428.68	429.88	323.57	322.33	329.74	323.57	322.33	323.57	323.57
356	355	356	262	261	267	263	262	262	263
			0.25						

$Y_{O_2,2}$	0.233	0.233	0.233	0.233	0.233	0.233	0.233	0.233	0.233	0.233
Fuel Flow Rate (<i>mL/min</i>)	21.01	21.01	21.01	20.96	21.30	16.63	16.69	16.63	16.55	16.50
P (<i>Pa</i>)	101300	101300	101300	101300	101300	101300	101300	101300	101300	101300
T_1 (<i>K</i>)	533.15	533.15	533.15	533.15	533.15	533.15	533.15	533.15	533.15	533.15
T_2 (<i>K</i>)	295.15	295.15	295.15	295.15	295.15	295.15	295.15	295.15	295.15	295.15
v_1 (<i>m/s</i>)	1.12	1.12	1.12	1.12	1.14	1.06	1.06	1.06	1.06	1.05
v_2 (<i>m/s</i>)	10.67	10.67	10.67	10.65	10.82	9.7	9.67	9.7	9.65	9.62
ρ_1 (<i>kg/m³</i>)	1.07	1.07	1.76	1.76	1.067	1.002	1.002	1.002	1.002	1.002
ρ_2 (<i>kg/m³</i>)	1.19	1.19	1.19	1.19	1.19	1.19	1.19	1.19	1.19	1.19
a_1 (<i>1/s</i>)	450.53	450.53	450.53	449.47	456.86	422.895	421.80	422.85	420.72	419.62
a_2 (<i>1/s</i>)	428	427	427	426	433	388	387	389	386	386
$Y_{F,1}$	0.5					0.45				

- n-decane

0.233	0.233	0.233	0.233	0.233	0.233	0.233	0.233	0.233	0.233	0.233	0.233	0.233
16.50	12.75	12.64	12.64	12.64	12.67	9.49	9.36	9.39	9.43	9.49	6.87	
101300	101300	101300	101300	101300	101300	101300	101300	101300	101300	101300	101300	101300
533.15	533.15	533.15	533.15	533.15	533.15	533.15	533.15	533.15	533.15	533.15	533.15	533.15
295.15	295.15	295.15	295.15	295.15	295.15	295.15	295.15	295.15	295.15	295.15	295.15	295.15
1.05	0.97	0.96	0.96	0.96	0.96	0.86	0.86	0.86	0.86	0.87	0.78	
9.62	8.65	8.55	8.55	8.55	8.575	7.55	7.45	7.47	7.5	7.55	6.55	
1.002	0.94	0.94	0.96	0.94	0.94	0.89	0.89	0.89	0.89	0.89	0.84	
1.19	1.19	1.19	1.19	1.19	1.19	1.19	1.19	1.19	1.19	1.19	1.19	
419.62	387.67	384.29	384.29	384.29	385.42	349.24	344.62	345.77	346.93	349.24	311.33	
386	346	343	342	343	344	303	299	300	300	302	262	
	0.4					0.35					0.3	

0.233	0.233	0.233	0.233	0.233	0.233	0.233	0.233	0.233
6.87	6.87	6.87	6.89	4.51	4.45	4.45	4.47	4.47
101300	101300	101300	101300	101300	101300	101300	101300	101300
533.15	533.15	533.15	533.15	533.15	533.15	533.15	533.15	533.15
295.15	295.15	295.15	295.15	295.15	295.15	295.15	295.15	295.15
0.78	0.78	0.78	0.78	0.65	0.64	0.65	0.65	0.64
6.55	6.55	6.55	6.57	5.3	5.22	5.2	5.25	5.25
0.84	0.84	0.84	0.84	0.8	0.8	0.8	0.8	0.8
1.19	1.19	1.19	1.19	1.19	1.19	1.19	1.19	1.19
311.33	311.33	311.33	312.52	258.49	254.84	254.84	256.06	256.06
262	262	262	263	213	209	210	211	211
				0.25				

$Y_{O_2,2}$	0.233	0.233	0.233	0.233	0.233	0.233	0.233	0.233	0.233	0.233
Fuel Flow Rate (<i>mL/min</i>)	17.49	17.56	17.54	17.74	17.74	13.52	13.39	13.39	13.39	13.31
P (<i>Pa</i>)	101300	101300	101300	101300	101300	101300	101300	101300	101300	101300
T_1 (<i>K</i>)	533.15	533.15	533.15	533.15	533.15	533.15	533.15	533.15	533.15	533.15
T_2 (<i>K</i>)	295.15	295.15	295.15	295.15	295.15	295.15	295.15	295.15	295.15	295.15
v_1 (<i>m/s</i>)	0.94	0.94	0.94	0.95	0.95	0.86	0.85	0.85	0.85	0.85
v_2 (<i>m/s</i>)	0.9	0.9	0.9	0.9	0.9	0.8	0.79	0.79	0.79	0.79
ρ_1 (<i>kg/m³</i>)	1.09	1.09	1.09	1.09	1.09	1.03	1.03	1.03	1.03	1.03
ρ_2 (<i>kg/m³</i>)	1.19	1.19	1.19	1.19	1.19	1.19	1.19	1.19	1.19	1.19
a_1 (<i>1/s</i>)	374.66	376.74	375.69	379.86	379.86	344.77	341.54	341.54	341.54	339.38
a_2 (<i>1/s</i>)	362	363	361	365	365	320	319	318	318	316
$Y_{F,1}$	0.5					0.45				

- n-dodecane

0.233	0.233	0.233	0.233	0.233	0.233	0.233	0.233	0.233	0.233	0.233	0.233	0.233
10.61	10.47	10.43	10.43	10.61	8.08	8.20	8.18	8.21	8.3	4.68	5.58	
101300	101300	101300	101300	101300	101300	101300	101300	101300	101300	101300	101300	101300
533.15	533.15	533.15	533.15	533.15	533.15	533.15	533.15	533.15	533.15	533.15	533.15	533.15
295.15	295.15	295.15	295.15	295.15	295.15	295.15	295.15	295.15	295.15	295.15	295.15	295.15
0.81	0.80	0.79	0.79	0.81	0.75	0.76	0.76	0.76	0.78	0.53	0.64	
0.73	0.72	0.72	0.72	0.73	0.65	0.66	0.66	0.66	0.67	0.45	0.54	
0.96	0.96	0.96	0.96	0.96	0.9	0.9	0.9	0.9	0.9	0.85	0.85	
1.19	1.19	1.19	1.19	1.19	1.19	1.19	1.19	1.19	1.19	1.19	1.19	
324.96	320.51	319.39	319.39	324.96	300.58	305.17	304.02	305.17	308.61	214.88	256.20	
292	290	289	287	293	262	267	266	267	270	182	222	
0.4					0.35					0.3		

0.233	0.233	0.233	0.233	0.233	0.233	0.233	0.233	0.233
5.7	5.63	5.63	5.6	2.94	2.85	2.89	2.81	2.83
101300	101300	101300	101300	101300	101300	101300	101300	101300
533.15	533.15	533.15	533.15	533.15	533.15	533.15	533.15	533.15
295.15	295.15	295.15	295.15	295.15	295.15	295.15	295.15	295.15
0.65	0.65	0.65	0.64	0.43	0.41	0.42	0.41	0.41
0.55	0.54	0.55	0.54	0.35	0.34	0.35	0.34	0.34
0.85	0.85	0.85	0.85	0.81	0.81	0.81	0.81	0.81
1.19	1.19	1.19	1.19	1.19	1.19	1.19	1.19	1.19
262.10	258.56	258.56	257.38	171.04	166.19	168.62	163.77	164.98
222	219	219	219	141	137	140	135	136
				0.25				

Autoignition

- n-heptane

Δ [K]	$Y_{O_2,2}$	$Y_{F,1}$	$T_{2,ign}$ [K]	$T_{2,ign}$ [K] with radiation loss	T_1 [K]	P [Pa]
57.35	0.233	0.4	1156.16	1213.52	533.15	101300
57.78	0.21	0.4	1158.30	1216.08	533.15	101300
58.09	0.19	0.4	1159.84	1217.93	533.15	101300
58.84	0.17	0.4	1163.57	1222.42	533.15	101300
59.68	0.15	0.4	1167.68	1227.36	533.15	101300
60.38	0.13	0.4	1171.06	1231.43	533.15	101300
60.98	0.11	0.4	1173.95	1234.93	533.15	101300
62.00	0.09	0.4	1178.82	1240.82	533.15	101300
62.95	0.07	0.4	1183.29	1246.25	533.15	101300
Δ [K]	$Y_{F,1}$	$Y_{O_2,2}$	$T_{2,ign}$ [K]	$T_{2,ign}$ [K] with radiation loss	T_1 [K]	P [Pa]
55.97	0.5	0.233	1149.16	1205.12	533.15	101300
56.77	0.45	0.233	1153.24	1210.01	533.15	101300
57.17	0.4	0.233	1155.24	1212.41	533.15	101300
57.58	0.35	0.233	1157.31	1214.89	533.15	101300
58.47	0.3	0.233	1161.71	1220.18	533.15	101300
59.30	0.25	0.233	1165.84	1225.14	533.15	101300

- n-decane

Δ [K]	$Y_{O_2,2}$	$Y_{F,1}$	$T_{2,ign}$ [K]	$T_{2,ign}$ [K] with radiation loss	T_1 [K]	P [Pa]
59.52	0.233	0.4	1166.87	1226.39	533.15	101300
60.10	0.21	0.4	1169.71	1229.80	533.15	101300
60.42	0.19	0.4	1171.26	1231.68	533.15	101300
60.89	0.17	0.4	1173.52	1234.42	533.15	101300
61.51	0.15	0.4	1176.47	1237.98	533.15	101300
62.00	0.13	0.4	1178.82	1240.82	533.15	101300
62.48	0.11	0.4	1181.09	1243.58	533.15	101300
63.74	0.09	0.4	1186.95	1250.69	533.15	101300
65.18	0.07	0.4	1193.60	1258.78	533.15	101300
Δ [K]	$Y_{F,1}$	$Y_{O_2,2}$	$T_{2,ign}$ [K]	$T_{2,ign}$ [K] with radiation loss	T_1 [K]	P [Pa]
58.44	0.5	0.233	1161.57	1220.01	533.15	101300
58.96	0.45	0.233	1164.16	1223.13	533.15	101300
59.54	0.4	0.233	1166.99	1226.53	533.15	101300
60.35	0.35	0.233	1170.90	1231.25	533.15	101300
60.94	0.3	0.233	1173.78	1234.73	533.15	101300
62.15	0.25	0.233	1179.50	1241.64	533.15	101300

- n-dodecane

Δ [K]	$Y_{O_2,2}$	$Y_{F,1}$	$T_{2,ign}$ [K]	$T_{2,ign}$ [K] with radiation loss	T_1 [K]	P [Pa]
61.85	0.233	0.4	1178.08	1239.92	533.15	101300
62.64	0.21	0.4	1181.82	1244.46	533.15	101300
63.12	0.19	0.4	1184.09	1247.21	533.15	101300
63.34	0.17	0.4	1185.11	1248.46	533.15	101300
63.76	0.15	0.4	1187.05	1250.81	533.15	101300
64.16	0.13	0.4	1188.90	1253.06	533.15	101300
64.83	0.11	0.4	1192.00	1256.83	533.15	101300
65.97	0.09	0.4	1197.18	1263.16	533.15	101300
66.94	0.07	0.4	1201.51	1268.45	533.15	101300
Δ [K]	$Y_{F,1}$	$Y_{O_2,2}$	$T_{2,ign}$ [K]	$T_{2,ign}$ [K] with radiation loss	T_1 [K]	P [Pa]
60.34	0.5	0.233	1170.88	1231.22	533.15	101300
61.34	0.45	0.233	1175.67	1237.01	533.15	101300
62.08	0.4	0.233	1179.20	1241.29	533.15	101300
63.02	0.35	0.233	1183.61	1246.62	533.15	101300
63.78	0.3	0.233	1187.17	1250.95	533.15	101300
65.04	0.25	0.233	1192.96	1258.00	533.15	101300

- n-heptane

Δ [K]	$Y_{O_2,2}$	$Y_{F,1}$	$T_{2,ign}$ [K]	$T_{2,ign}$ [K] with radiation loss	T_1 [K]	P [Pa]
59,83	0.233	0.4	1168,40	1228,23	473.15	101300
60,29	0.21	0.4	1170,65	1230,95	473.15	101300
60,65	0.19	0.4	1172,36	1233,00	473.15	101300
61,29	0.17	0.4	1175,44	1236,73	473.15	101300
61,70	0.15	0.4	1177,39	1239,10	473.15	101300
62,70	0.13	0.4	1182,12	1244,82	473.15	101300
63,04	0.11	0.4	1183,71	1246,75	473.15	101300
63,98	0.09	0.4	1188,10	1252,08	473.15	101300
64,68	0.07	0.4	1191,29	1255,96	473.15	101300
Δ [K]	$Y_{F,1}$	$Y_{O_2,2}$	$T_{2,ign}$ [K]	$T_{2,ign}$ [K] with radiation loss	T_1 [K]	P [Pa]
58,96	0.5	0.233	1164,16	1223,12	473.15	101300
59,54	0.45	0.233	1166,98	1226,52	473.15	101300
59,93	0.4	0.233	1168,88	1228,81	473.15	101300
60,59	0.35	0.233	1172,09	1232,69	473.15	101300
61,38	0.3	0.233	1175,87	1237,25	473.15	101300
62,31	0.25	0.233	1180,29	1242,60	473.15	101300

- n-decane

Δ [K]	$Y_{O_2,2}$	$Y_{F,1}$	$T_{2,ign}$ [K]	$T_{2,ign}$ [K] with radiation loss	T_1 [K]	P [Pa]
62,86	0.233	0.4	1182,87	1245,74	473.15	101300
63,20	0.21	0.4	1184,45	1247,65	473.15	101300
63,60	0.19	0.4	1186,30	1249,90	473.15	101300
64,07	0.17	0.4	1188,48	1252,55	473.15	101300
64,59	0.15	0.4	1190,89	1255,49	473.15	101300
65,42	0.13	0.4	1194,67	1260,08	473.15	101300
66,04	0.11	0.4	1197,49	1263,53	473.15	101300
66,60	0.09	0.4	1200,02	1266,63	473.15	101300
67,79	0.07	0.4	1205,34	1273,13	473.15	101300
Δ [K]	$Y_{F,1}$	$Y_{O_2,2}$	$T_{2,ign}$ [K]	$T_{2,ign}$ [K] with radiation loss	T_1 [K]	P [Pa]
61,94	0.5	0.233	1178,53	1240,47	473.15	101300
63,11	0.45	0.233	1184,04	1247,16	473.15	101300
63,98	0.4	0.233	1188,07	1252,05	473.15	101300
64,50	0.35	0.233	1190,48	1254,98	473.15	101300
65,02	0.3	0.233	1192,83	1257,85	473.15	101300
66,05	0.25	0.233	1197,52	1263,57	473.15	101300